Nonlinear dynamics of premixed flames: from deterministic stages to stochastic influence

B. Radisson[1,2], **B. Denet**[1] **and C. Almarcha**[1],†

[1]Aix-Marseille Université, CNRS, École Centrale Marseille, Institut de Recherche sur les Phénomènes Hors Équilibre, UMR 7342, 49 rue F. Joliot Curie, 13013 Marseille, France

[2]Department of Aerospace and Mechanical Engineering, University of Southern California, Los Angeles, CA 90089-1191, USA

Premixed flame propagation is a rich interface problem. Instabilities and nonlinearities lead to the formation of cusps pointing toward the burnt gas. These cusps, which undergo complex dynamics, enhance the reaction rate by increasing the flame surface. These crests can be interpreted as pole solutions of the Michelson–Sivashinsky equation that evolve according to ordinary differential equations. Thanks to a quasi-bidimensional experimental facility (a Hele-Shaw burner) we evaluate the accuracy of the description of flame dynamics by elementary interaction between cusps. In particular, we address the time for which a direct comparison between experiments and numerical integration is feasible. The sensitivity to initial conditions and noise is discussed. We demonstrate that at any time of evolution, interesting features can be recovered by describing the flame surface evolution as pole dynamics.

Key words: pattern formation, flames

1. Introduction

In their experiments on explosions in coal mines, Mallard & Le Chatelier (1883) reported for the first time the observation of the cellular nature of premixed flames. Since this pioneering work, many other experimental studies have confirmed this particular phenomenon (Smithells & Ingle 1892; Groff 1982; Bradley 1999). In two similar independent studies Darrieus (1938) and Landau (1944) proposed that the exothermic character of combustion is responsible for a hydrodynamic instability that leads to this corrugated pattern. By considering the front as a discontinuity between two inviscid flows of different densities and by using appropriate Rankine–Hugoniot conditions (see Landau & Lifshitz (1959), chapter IX § 84), they performed a linear stability analysis and demonstrated that the front is unconditionally unstable, with a linearly increasing growth rate with respect to the wavenumber of the perturbation. By introducing a flame curvature dependence of the local flame speed, Markstein (1951) managed to take flame thickness effects into account and obtained a dispersion relation for flames of finite thickness

$$\sigma = 4\frac{\sigma_M}{k_c}\left(|k| - \frac{k^2}{k_c}\right), \tag{1.1}$$

† Email address for correspondence: almarcha@irphe.univ-mrs.fr

where σ and k are, respectively, the growth rate and the wavenumber of the perturbation, σ_M is the growth rate of the most unstable wavelength and k_c is a cutoff wavenumber. By introducing this new formalism and considering the gravity effect, Markstein reconciled the linear stability theory with experimental observations of downwards planar propagating flames (Quinard 1984; Searby & Quinard 1990). In particular, he pointed out that there is a small cutoff wavelength $\lambda_c = 2\pi/k_c$ due to thermal diffusion and a large cutoff wavelength caused by the stabilizing effect of gravity (Taylor 1950; Markstein 1951; Pelce & Clavin 1982).

By looking at flames propagating in glass tubes, Markstein (1949) also noted that the flame destabilization quickly leads to cellular patterns with stationary amplitude. As first identified by Karlovitz, Denniston & Wells (1951) and Manton, von Elbe & Lewis (1952), this saturation has a nonlinear Huygens geometrical origin. Due to the normal propagation of the front, the radius of curvature increases (decreases) where the front is convex (concave) toward the unburned gases, leading to cells separated by abrupt cusps. Then, as a consequence of the flow induced in the unburned gas, this cellular pattern exhibits complex dynamics with larger cells growing at the expense of smaller neighbours in a way similar to bubbles competition in water (Layzer 1955). Numerical experiments either in the small expansion framework (Michelson & Sivashinsky 1977; Creta, Fogla & Matalon 2011) or with a fully nonlinear model (Rastigejev & Matalon 2006*a*; Creta & Matalon 2011; Altantzis *et al.* 2012) have shown that these dynamics can lead to a final monocellular solution with characteristic sizes much larger than the most unstable wavelength $\lambda_{max} = 2\lambda_c$ predicted by the linear theory (Markstein 1949). These observations highlight the importance of the geometrical nonlinear effects in the long-time dynamics. Indeed, by forming a unique large cell stabilized by stretch (Uberoi 1959), the hydrodynamic instability is responsible for a new stable state (Zeldovich *et al.* 1980; Pelce & Clavin 1987; Rabaud, Couder & Gerard 1988).

However, as observed in Markstein's experiments, for flames propagating in large vessels the merging process of cells is permanently supplied by the appearance of smaller cells (Michelson & Sivashinsky 1977; Gutman & Sivashinsky 1990; Rahibe *et al.* 1995; Rastigejev & Matalon 2006*a*; Creta *et al.* 2011; Altantzis *et al.* 2012; Yu, Bai & Bychkov 2015) created by splitting cells, after they reached an excessive size. This process never leads to the steady monocellular arrangement observed in smaller experiments (Uberoi 1959; Von Lavante & Strehlow 1983; Pelcé-Savornin, Quinard & Searby 1988). As first suggested by Joulin (1989), these new crest formations are caused by the background noise that generates small wrinkles on the front that are in turn magnified by the Darrieus–Landau instability.

Hence, the dynamics of premixed flames results from the competition between several intrinsic properties (large-scale hydrodynamic coupling, thermodiffusive phenomena, geometrical nonlinear effects) and external stochastic forcing (hydrodynamics or thermal perturbations). Recently, by studying flames propagating in a Hele-Shaw burner, Almarcha *et al.* (2018) have shown that a small expansion model (Sivashinsky 1977) provides a good description of the flame evolution both during the destabilization process and the long-time evolution. In particular, they demonstrated that the dynamics is accurately described by the trajectories of poles associated with the analytical solutions of the Michelson–Sivashinsky (MS) equation, up to a certain time. Beyond this time, the stochastic influence of the background noise becomes important and the system can no longer be described as a deterministic process. However, the pole-to-pole interaction still holds locally and allows us to predict some statistical properties of the flame front.

The aim of the present paper is to extend this previous work, in particular to characterize the typical time under which the flame dynamics remains deterministic, and to assess the validity of the statistical description at large time by comparing numerical, experimental and analytical results.

Compared to some of our recent papers, such as Al Sarraf *et al.* (2018*a*) and Almarcha *et al.* (2018), we have greatly improved the experimental techniques, which will allow us to study the repeatability of experiments and perform successful comparisons with theoretical results, both on the short-time nonlinear evolution and on the long-time statistical properties of the front.

The paper is organized as follows. In § 2 the experimental set-up used for this work is described, with special consideration given to its benefits and limitations. Then, early deterministic regimes of destabilization, nonlinear saturation and deterministic pole interaction are analysed in § 3 by way of the MS model whose relevance with regards to laboratory experiments is underlined. Finally, under the influence of stochastic external forcing, the statistical features of the flame topology are described in § 4.

2. Experimental set-up

Most of the experimental studies about intrinsic flame instability and dynamics are based on anchored inverted V-flames (Truffaut & Searby 1999) or flame propagation in expanding flame balls (Bradley 1999; Jomaas, Law & Bechtold 2007) or in glass tubes (Markstein 1949; Quinard 1984; Clanet & Searby 1998; Almarcha, Denet & Quinard 2015). In the first configuration, the angle between the front and the mean flow, implies the existence of a tangential velocity component. The wrinkles are advected along the front and the time over which their dynamics can be studied is limited. In the two other configurations, although long-time dynamics can be observed, the analysis of the front properties is difficult due to the three-dimensional character of the reaction sheet. In the present study, in order to avoid these shortcomings, the dynamics of the flame is analysed in a Hele-Shaw burner. The later was first proposed in the framework of an analytical study by Joulin & Sivashinsky (1994) and introduced experimentally by Sharif, Abid & Ronney (1999). The apparatus consists of two vertically oriented borosilicate glass plates, 0.5 m wide and 1.5 m high, separated by a 5 mm gap, closed on the sides, open at the top and supplied with a premixed mixture at the bottom. The gap between the plates being of the order of the cutoff wavelength λ_c (depending on the equivalence ratio), this burner presents the major advantage of forcing the flame to be stationary in the thickness direction. Indeed, after a transient destabilization, the flame quickly moves toward a steady monocellular shape in the thickness direction. The dynamics is thus constrained in that direction and the analysis is significantly simplified into a bidimensional evolution. In the following sections we discuss in detail the choice of the main characteristics of this experimental apparatus.

2.1. *Experimental procedure*

For each experiment reported in the present study, the same operating procedure is used for each run. A flow of the combustible mixture, adjusted to the desired equivalence ratio (φ) and dilution ($\delta = V_{O_2}/(V_{O_2} + V_{N_2})$) with less than 1 % error thanks to a PC-interface connected to Bronkhorst EL-Flow series mass-flow regulators, is maintained from bottom to top until there is complete homogenization in the burner. A two-dimensional inverted V-flame is ignited at the top of the burner and remains anchored as the flow rate exceeds the flame velocity, until the flow is stopped by closing a valve upstream. The flame then starts its downwards propagation (recorded using a high-speed camera), from an initially
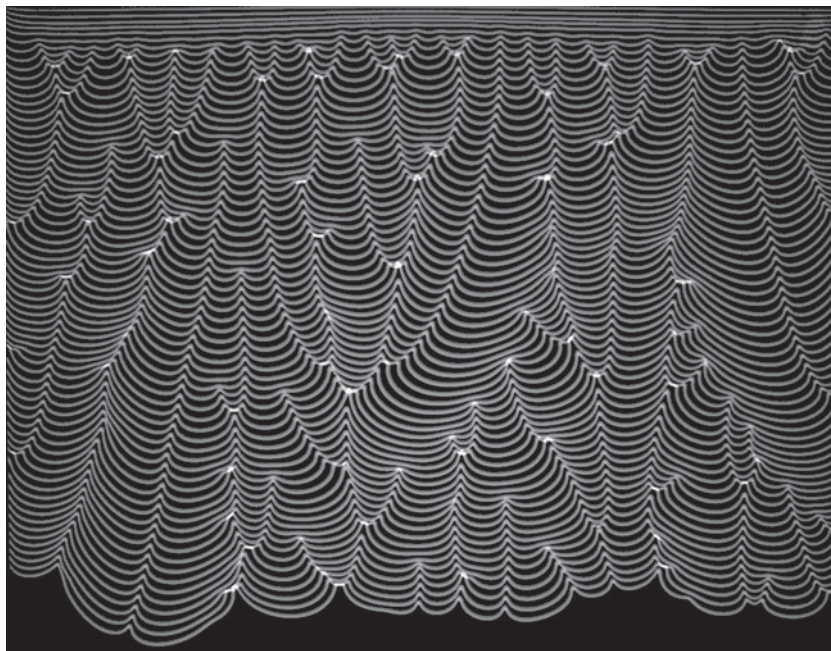
FIGURE 1. Spatiotemporal diagram of a propane–air flame ($\varphi = 0.8$) propagating downwards in a Hele-Shaw burner. Field of view width is 46 cm. Time between two successive fronts is 14 ms. The front starts flat and is rapidly destabilized due to the Darrieus–Landau effect. Rapidly the instability is saturated by nonlinearities and a complex dynamics is observed. The crest merging and crest creations are readily visible.

flat state that quickly leads to a cellular pattern due to hydrodynamic destabilizing effects (see figure 1).

2.2. *Design of the burner*

2.2.1. *Thickness*

The thickness of the burner is of prime importance. On one hand it must be thin enough to guarantee that the flame has a steady profile in the burner thickness direction. On the other hand, if the thickness is not large enough, momentum (Saffman & Taylor 1958) and heat losses at the wall may completely modify the standard Darrieus–Landau picture. By measuring the flame propagation for stoichiometric propane–air flames in small channels (Gutkowski & Jarosiński 2009) or in a Hele-Shaw burner (Jang, Jang & Kim 2018), it has been shown that by decreasing channel width, the flame speed is first slightly increased up to a channel thickness around 5 mm due to surface incremental increase with curvature in the thickness. Then for smaller channel widths, as heat losses become dominant, the flame speed is strongly decreasing with the thickness of the burner until it reaches a quenching thickness ($\approx$2 mm). For propane–air flames the 5 mm thickness seems to be a good compromise. This choice was confirmed in the same apparatus by the Al Sarraf *et al.* (2018*a*) growth rate measurements that follow the standard $\sigma \sim k - k^2$ (1.1) dispersion relation for all mixture compositions. The latter result shows that even if the heat and momentum losses due to the confinement of the flame may modify the coefficients in
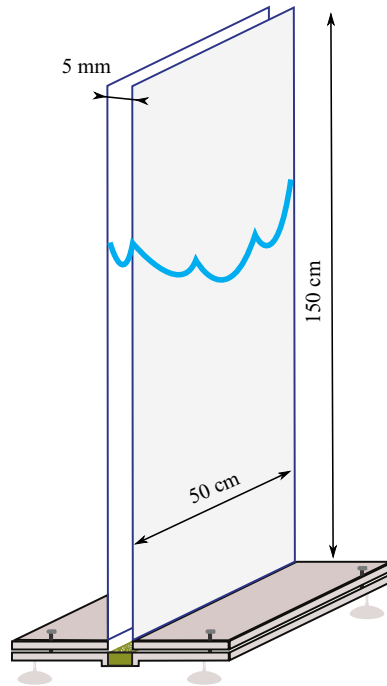
FIGURE 2. Sketch of the experimental apparatus used in this study. The two glass plates are vertically oriented and separated by a thin gap closed on the sides and at the bottom. The burner is filled with an homogeneous mixture of propane and air at desired equivalence ratio φ and dilution δ (see § 2.1 for definition). The flame is ignited at the top and propagates downwards.

the dispersion relation, the underlying mechanisms governing the dynamics of the flame remain the same as for the three-dimensional configuration (Clanet & Searby 1998).

2.2.2. *Width*

The width of the cell has to be sufficiently large so that the side walls do not impact the flame behaviour in the middle of the cell. The mean size of the pattern expected in the late-time dynamics is approximately a few times (Cambray, Joulain & Joulin 1994) the maximum unstable wavelength (approximately 1 cm here). In order to get a sufficient number of cells for the late-time regime studied in § 4, we use a burner 10 times larger than this mean cell size, i.e. 50 cm wide (figure 2).

2.2.3. *Height*

As the flame propagates from top to bottom, the height of the burner imposes the time over which the flame propagation can be studied. As we are interested in both the short- and long-time dynamics, the apparatus should be high enough to guarantee that the flame reaches a fully developed stage. Due to nonlinear interaction, this time can be significantly longer than the characteristic time of the instability $t_\sigma = 1/\sigma_{max}$ (Joulin & Cambray 1992). Considering a typical $t_\sigma \sim 10^{-2}$ s (Al Sarraf *et al.* 2018*a*) and a typical flame propagation speed $u_T \sim 1$ m s^{-1}, the time for the flame to propagate from top to bottom of the 1.5 m high burner, is of the order $\sim 10^2 t_\sigma$.
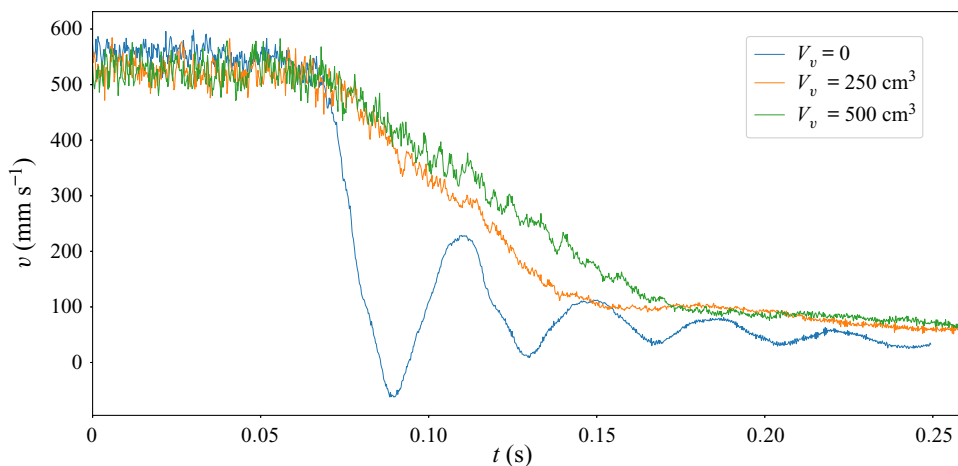
FIGURE 3. Evolution of the vertical speed of the flow after the valve closure for three different set-ups. After a delay time (0.7 s) corresponding to the closure time of the solenoid valve, the deceleration of the flow is observed.

2.2.4. *Valve closure system*

The short-time destabilization is likely to be altered by the gas deceleration after closing the valve. The closure system must be carefully designed to avoid undesirable buoyancy effects including Rayleigh–Taylor instability (Taylor 1950). In order to characterize the acceleration experienced by the gas after the valve closure, we measure the evolution of the flow speed by using particle image velocimetry. For this purpose, a continuous 532 nm laser sheet is placed in the Hele-Shaw burner and the mixture flow is seeded with oil droplets. We perform repeatable experiments using a solenoid valve (contrary to the Al Sarraf *et al.* (2018*a*) study where the flow was stopped manually). When the valve is closed, it triggers a high-speed camera that records the flow deceleration. The velocity field is then obtained by a particle image velocimetry cross-correlation algorithm (Meunier & Leweke 2003). The vertical velocity of the flow is measured at one point at the top of the burner, a few centimetres inside. A vessel (of volume V_v) can be placed between the valve and the burner, in order to modify the decay rate of the flow. The evolution of the vertical velocity is plotted in figure 3 for three different values of V_v. As can be seen, when $V_v = 0$, the system behaves as an underdamped oscillator (see figure 3 (blue curve)) and the flame experiences strong acceleration effects ($\simeq 4g$) which are not desirable for an intrinsic flame dynamics analysis. The underlying mechanism for these oscillations is beyond the scope of the present paper and was studied in a recent paper (Radisson, Piketty-Moine & Almarcha 2019). However, to avoid these shortcomings, for all the experiments reported hereafter, a vessel $V_v = 250$ cm^3 is placed between the valve and the burner. In this way, the measured deceleration of the flow is approximately half the magnitude of gravity (see figure 3 (orange curve)), ensuring that Rayleigh–Taylor effects are negligible.

2.3. *Flammability limits*

The propane–air mixture was varied in order to explore the full range of equivalence ratios, up to the flammability limits of the apparatus, that allow the propagation of a flame. For the burner at ambient temperature $\approx$293 K the flammability limits were found to be

approximately $\varphi \approx 0.65$ on the lean side and $\varphi \approx 1.5$ on the rich side. The present work is limited to a range of equivalence ratios far from these extinction limits ($0.8 < \varphi < 1.3$).

2.4. *Data acquisition*

The flame dynamics are analysed by recording flame chemiluminescence images with a 8-bit high-speed video camera (Photron FASTCAM MINI AX 200) (figure 1). The flame-front coordinates are then extracted from these images by way of Python image processing (open-source library Scikit-Image) with subpixel accuracy.

3. Deterministic dynamics

In figure 1, two typical stages are clearly visible. Starting from an initially flat flame, some wrinkles first emerge and grow to form crests with saturated amplitude. In a second stage, these crests evolve in a complex motion including crest merging and new crest creations. In this section, we analyse the linear stage and then compare the evolution of the front with a nonlinear model and its analytical solutions. We also evaluate the time during which the trajectories of crests are deterministic.

3.1. *Growth rate measurements*

The unstable nature of flames is unveiled by the linear destabilization, starting from an initially flat flame. This is easily obtained in our experiment as the flame is anchored on the straight upper edge of the cell (figure 4) before it starts entering the cell. In that case, the most unstable wavelength emerges. However, in order to access the dispersion relation and the key features exposed on (1.1), it is necessary to start from an initial condition (figure 5) forced to develop selected wavelengths by using the forcing method introduced in Al Sarraf *et al.* (2018*a*). This procedure allows us to measure the growth rate of distinct wavelengths. Contrary to the Al Sarraf *et al.* (2018*a*) study, the burner supply line is now equipped with a solenoid valve which allows us to perform experiments in a repeatable way and the forcing plates are more accurately machined (we use for measuring growth rates a sinusoidal profile obtained by laser cutting). These improvements of experimental techniques allow us to present a new extended set of growth rate measurements and particularly to obtain a more precise value of the cutoff wavenumber. This better confidence on the k_c value will be of particular importance for the results presented in the next sections. The data obtained from these measurements are shown in figure 6. The theoretical dispersion relation (1.1) is then fitted with σ_M, the growth rate of the most unstable wavelength, and k_c, the cutoff wavenumber. As predicted by Sivashinsky (1977), we will show that the overall dynamics observed in our experiments can be described knowing these two parameter values.

3.2. *Saturation*

As evidenced by the flame-front evolution in figure 5, the exponential growth is rapidly saturated by a geometrical effect: the normal propagation of the front. This nonlinear effect is responsible for the formation of crests that limit the wrinkles' amplitude. Therefore, a relevant investigation of the physical mechanisms involved in the long-time dynamics requires nonlinear analysis with all the basic ingredients highlighted before: large-scale hydrodynamic instability, thermal restabilization at short wavelength and nonlinear geometrical effects able to saturate the instability. Carrying these three essential basic features and possessing the obvious advantage of being analytically tractable,
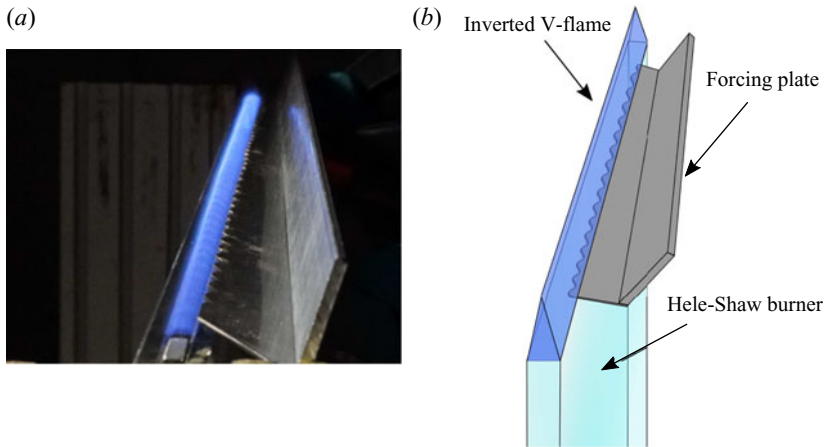
(*a*) (*b*)

FIGURE 4. Sketch of the experimental set-up used to perform growth rate measurements.
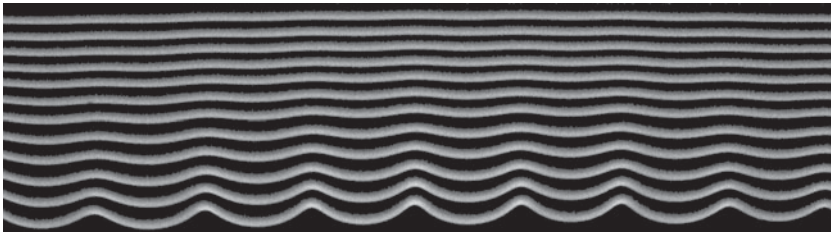

FIGURE 5. Unstable mode growth record in the first instants of propagation after stopping the flow (field of view 158 mm). Propane–air flame $\varphi = 0.8$. (Fronts have been artificially shifted to distinguish each time of evolution. Time between each front $dt = 7.5$ ms.) Here the flame is initially forced with a 18 mm wavelength. See Al Sarraf *et al.* (2018*a*) for details about forcing methods.

the MS equation (Sivashinsky 1977) seems to be an ideal candidate to allow a detailed description of the flame dynamics. In the following section, the model and its analytical solutions are first introduced and their essential properties are recalled. Its relevance regarding the experiments is then demonstrated.

3.3. *An asymptotic model: the MS equation*

Considering an infinitesimal thickness flame separating two inviscid flows of different densities and a kinematic relation with a linear dependence on flame-front curvature for the local flame speed, Sivashinsky (1977) showed that it is possible to obtain an evolution equation for the flame front. By performing an asymptotic development of the full set of equations in the limit of small expansion parameter $\gamma \to 0$ ($\gamma = (\rho_u - \rho_b)/\rho_u$), the flame-front dynamics is reduced to a pseudodifferential equation governing the motion of the front. At first order in γ it takes the form

$$\phi_t + \frac{u_A}{2}\phi_x^2 = \frac{4\sigma_M}{k_c}\left(\frac{\phi_{xx}}{k_c} + I(\phi, x)\right), \tag{3.1}$$
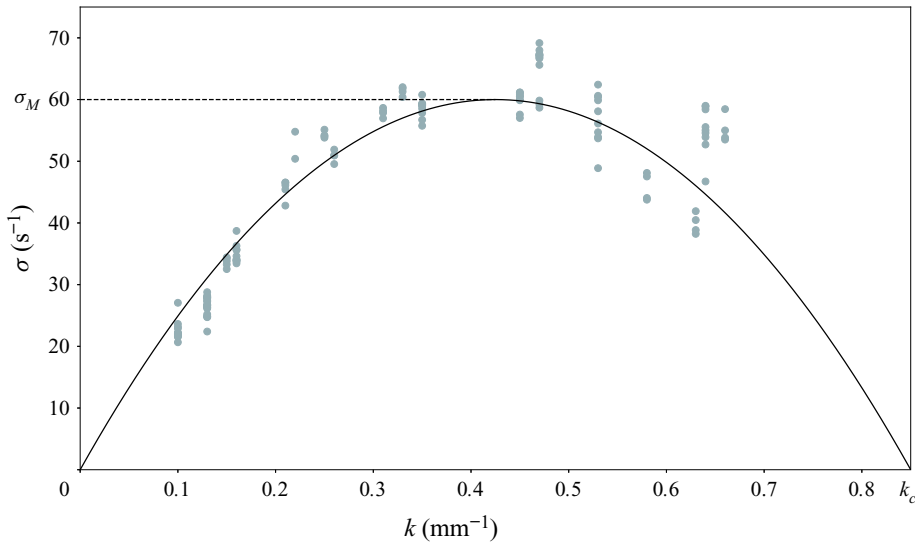
FIGURE 6. Growth rate measurements (downwards propagating propane–air flame $\varphi = 0.8$) obtained from flame dynamics analysis in the first instants of propagation. The experimental points are then fitted with the theoretical dispersion relation in order to determine the relevant σ_M and k_c parameters for our experiments.

where ϕ stands for the vertical position of the front, x is the transverse coordinate and t the time. Here, σ_M and u_A are parameters depending on the laminar flame speed and the expansion parameter γ. Here, k_c is the cutoff wavenumber depending on the reactive mixture properties and $I(\phi, x)$ is a linear operator given by

$$I(\phi, x) = \int_{-\infty}^{\infty} |k|\, \mathrm{e}^{\mathrm{i}kx} \hat{\phi}(k, t)\, \mathrm{d}k. \tag{3.2}$$

As can be seen in (3.1), from the first order in γ, the Sivashinsky model contains the three essential basic ingredients listed before. Moreover, it was shown later that despite new terms correcting the mean front displacement, this equation keeps almost the same functional structure up to second order (Sivashinsky & Clavin 1987; Joulin & Cambray 1992) and third order in γ (Kazakov 2005*a*,*b*) (stationary case). In (3.1), the last term is the instability term. Due to multiplication by $|k|$ in Fourier space, the $I(\phi, x)$ is responsible for the amplification of any disturbance with a linearly increasing growth rate with k the wavenumber of the perturbation. The curvature term ϕ_{xx} comes from the thermal diffusive restabilization and is responsible for the damping of disturbances at small scale. Finally, the ϕ_x^2 is a slope advection term and is responsible for the formation of cusps due to normal propagation of the front. In a way similar to the dynamics described by the Burgers equation, the cusps are regularized by the diffusive term in the right-hand side. These dynamics never lead to real slope singularity but to the formation of abrupt crests with rounded tips as can be seen in late stages of figure 5. As first shown by Bessis & Fournier (1984), these quasi-cusps can be expressed in term of complex singularities appearing in complex-conjugate pairs. Accordingly, the MS model admits analytical solutions which allow us to express the evolution of the flame front in terms of the trajectories of these complex singularities.
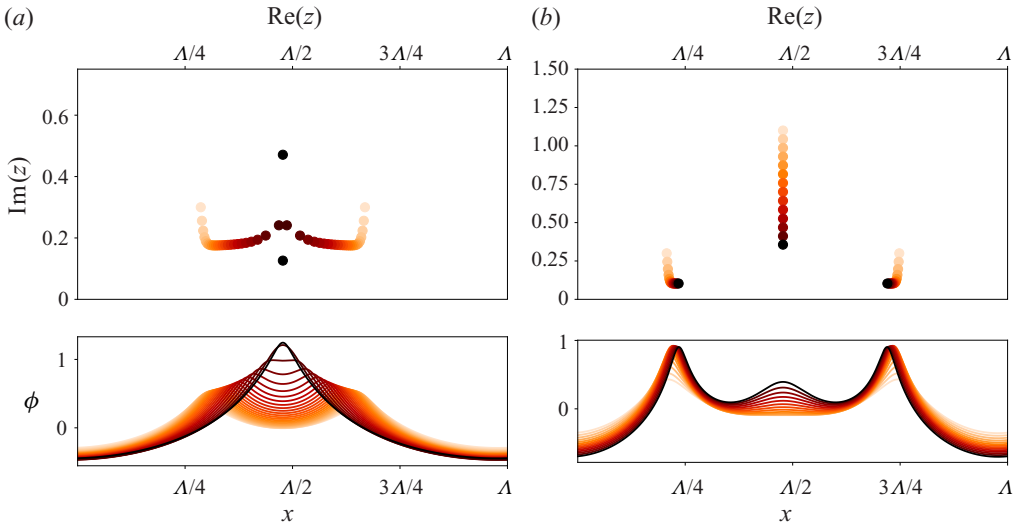
FIGURE 7. Evolution of arbitrary set of poles according to (3.4) and their corresponding solutions for the flame front (the time goes from the light initial condition to the dark final one). (*a*) Merging of two crests due to pole attraction along the real axis. (*b*) New crest creation due to attraction of a pole initially far from the real axis.

3.4. *Analytical pole solutions for the Sivashinsky equation*

As first noted by Thual, Frisch & Hénon (1985), the MS model belongs to a broader class of nonlinear models (Lee & Chen 1982) which admit analytical solutions in the form of complex pole decomposition: the solutions of (3.1) (with periodic boundary conditions) can be expressed as

$$\phi(x, t) = -\frac{8\sigma_M}{u_A k_c^2} \sum_{n=1}^{2N} \ln\left(\sin\left(\frac{\pi (x - z_n(t))}{\Lambda}\right)\right), \tag{3.3}$$

where Λ is the width of the domain, N is the number of complex conjugate pole pairs involved in the solution and z_n are the positions of the poles in the complex plane. Roughly speaking, each pair of poles is responsible for a distortion of the front around the abscissa $x = \text{Re}(z_n)$. The distortion is even more pronounced as $\text{Im}(z_n)$ is small ($\phi_x \to \pm\infty$ when $\text{Im}(z_n) \to 0$).

Substituting (3.3) in (3.1), the problem of the front dynamics is reduced to a dynamical system of $2N$ ordinary differential equations, that govern the poles trajectories in the complex plane,

$$\dot{z}_n = \frac{4\sigma_M}{k_c} \left[\frac{2\pi}{\Lambda k_c} \sum_{p \neq n} \cot\left(\frac{\pi}{\Lambda}\left(z_p - z_n\right)\right) - \mathrm{i}\, sign\left(\text{Im}(z_n)\right)\right], \tag{3.4}$$

where the first term in brackets is responsible for an attractive interaction between poles along the real axis, and a repulsive one along the imaginary axis. As each crest is the manifestation of at least one pair of poles in the complex plane, this horizontal attraction between poles is responsible for the crest merging observed in our experiments (see figure 1). Due to vertical repulsion, when two pairs of poles tend toward the same abscissa,
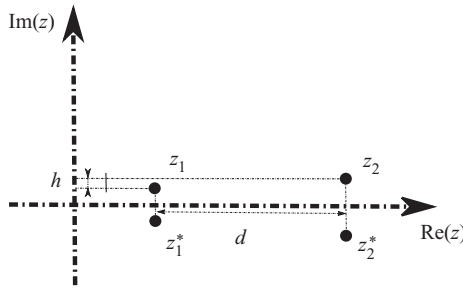
FIGURE 8. Interaction between two pairs of poles, sufficiently close to each other so that we can ignore interaction with other poles, but sufficiently far to have $h \ll d$ in order to consider a two-body interaction with a double charge (see (3.5)).

each of them follows an hyperbolic trajectory (Thual *et al.* 1985) in the complex plane and poles tend to align vertically forming giant crests (see the left part of figure 7). This pole dynamics leads to a steady giant cusp solution (the monocellular arrangement previously quoted) with all the poles aligned along the imaginary axis (Thual *et al.* 1985). This process is similar to the pole condensation in the Burgers equation and may be viewed as the mechanism leading to shock coalescence (see Bessis & Fournier 1984). In order to test the MS model and the accuracy of the pole solutions, we analyse the dynamics of a two cusps merging.

3.5. *Crest merging*

As in Almarcha *et al.* (2018), we are interested in the mechanism of cell fusion. We first present a formal derivation of the analytic law for cusp aggregation.

We consider two pairs of complex conjugate poles $z_1^{(*)} = x_1 \pm iy_1$ and $z_2^{(*)} = x_2 \pm iy_2$ sufficiently close to each other so that we can ignore their interaction with other poles (see figure 8). According to (3.4) and giving $C_1 = 4\sigma_M/kc$ and $C_2 = 2\pi/\Lambda k_c$, we have

$$
\Rightarrow
\begin{cases}
\dot{z}_1 = C_1 \left\{ C_2 \left[\cot\left(\frac{\pi}{\Lambda}(d+ih)\right) + \cot\left(\frac{\pi}{\Lambda}(d-il)\right) + \cot\left(-2i\frac{\pi}{\Lambda}y_1\right) \right] - i \right\}, \\
\dot{z}_2 = C_1 \left\{ C_2 \left[\cot\left(-\frac{\pi}{\Lambda}(d+ih)\right) + \cot\left(-\frac{\pi}{\Lambda}(d+il)\right) + \cot\left(-2i\frac{\pi}{\Lambda}y_2\right) \right] - i \right\}, \\
\dot{z}_1^* = C_1 \left\{ C_2 \left[\cot\left(\frac{\pi}{\Lambda}(d+il)\right) + \cot\left(\frac{\pi}{\Lambda}(d-ih)\right) + \cot\left(2i\frac{\pi}{\Lambda}y_1\right) \right] + i \right\}, \\
\dot{z}_2^* = C_1 \left\{ C_2 \left[\cot\left(-\frac{\pi}{\Lambda}(d-il)\right) + \cot\left(-\frac{\pi}{\Lambda}(d-ih)\right) + \cot\left(2i\frac{\pi}{\Lambda}y_2\right) \right] + i \right\},
\end{cases}
\tag{3.5}
$$

with

$$
\left.
\begin{aligned}
d &= x_2 - x_1, \\
h &= y_2 - y_1, \\
l &= y_2 + y_1,
\end{aligned}
\right\}
\tag{3.6}
$$

so that

$$
\Rightarrow \dot{d} = -C_1 C_2 \left\{ \cot\left(\frac{\pi}{\Lambda}(d+ih)\right) + \cot\left(\frac{\pi}{\Lambda}(d-ih)\right) \right.
$$
$$
\left. + \cot\left(\frac{\pi}{\Lambda}(d-il)\right) + \cot\left(\frac{\pi}{\Lambda}(d+il)\right) \right\}.
\tag{3.7}
$$

In the limit where poles are sufficiently close to each other so that we can ignore interaction with other poles, and where the two poles are near their equilibrium position along the imaginary axis (i.e. attraction due to second term in the right-hand side of (3.4) in equilibrium with the repulsive force due to interaction with their c.c $\Rightarrow h \ll \Lambda/\pi$ and $l \ll \Lambda/\pi$)

$$\Rightarrow \dot{d} = -\frac{2\Lambda C_1 C_2}{\pi d \left(1 + \left(\frac{h}{d}\right)^2\right)} - \frac{2\Lambda C_1 C_2}{\pi d \left(1 + \left(\frac{l}{d}\right)^2\right)}, \tag{3.8}$$

which yields, at leading order when $h/d \to 0$ and $l/d \to 0$, to

$$\Rightarrow d^2(t) = d_0^2 - \frac{8 C_1 C_2 \Lambda}{\pi} t = d_0^2 - \frac{64\sigma_M}{k_c^2} t. \tag{3.9}$$

The latter is equivalent to the interaction between two poles on the real axis, each of them having a double charge.

As each pole z is responsible for the presence of a crest at $x = \mathrm{Re}(z)$, the squared distance between two crests is a linearly decreasing function of t with a slope $d_t^2 = -64\sigma_M/k_c^2$. This theoretical law, already introduced by Almarcha *et al.* (2018) is now checked experimentally and numerically.

For this purpose, the pole dynamics ordinary differential equation (3.4) is integrated from an initial condition with two isolated poles with equal imaginary parts ($\mathrm{Im}(z_1) = \mathrm{Im}(z_2)$) (figure 9b). The evolution of the horizontal distance between the two poles ($d(t) = \mathrm{Re}(z_2) - \mathrm{Re}(z_1)$) is computed. On the other hand, an experimental merging of two isolated crests is analysed in the Hele-Shaw burner (figure 9a), and the evolution of the distance between them $d(t) = \sqrt{(x_r - x_l)^2 + (y_r - y_l)^2}$ is computed. These two evolutions are then compared with the asymptotic law (3.9) using σ_M and k_c values obtained in § 3.1 (see right part of figure 9). As can be seen, the experiment not only corroborates the functional form of (3.9) but also the value of the slope, which was not obtained in Almarcha *et al.* (2018), due to a low precision on the cutoff wavenumber. This good agreement underlines the relevance of pole description for real flames.

3.6. *Crest creation*

In viscous Burgers dynamics, shocks are relaxed by pole repulsion to $\pm i\infty$. In MS dynamics, instead, the second term in brackets in (3.4), is responsible for an attraction of poles toward the real axis. Due to this instability term, poles that are initially far from the real axis (therefore not visible on the front solution) may drift toward the real axis. This mechanism can be responsible for the appearance of new crests (see the right part of figure 7). However, in our experiments we observe permanent new crest creation during the flame propagation (see figure 1), which could be seen as the presence of an infinite ($N \to \infty$) reservoir of poles initially far from the real axis. On the other hand if N is finite, the pole dynamics cannot describe the experimental observations for large times. The problem of new crest creations is therefore of fundamental importance to settle whether our experiments can be described by a purely deterministic model such (3.4). To make the discussion about new crest creations simpler (and simplify the comparison between the numerical experiments in § 4.1.1 and the other ones from the literature), we introduce the non-dimensional MS equation. Introducing $\Lambda = 2\pi/K$ the width of the
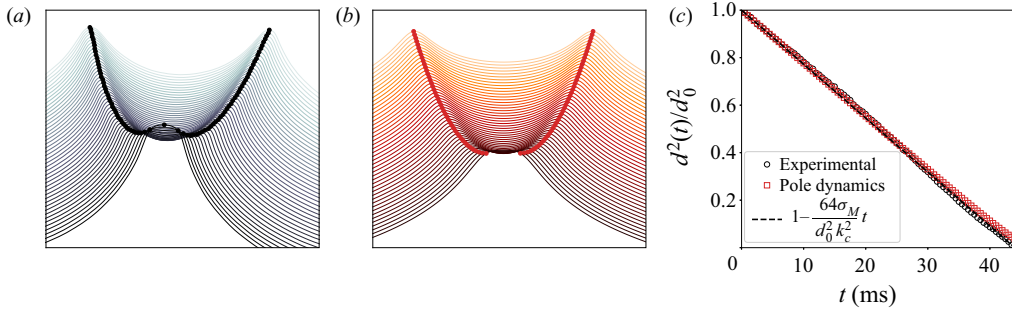
FIGURE 9. Merging process between two isolated crests of a propane–air flame ($\varphi = 0.8$). (*a*) Successive fronts extracted from an experimental movie during the merging process. Time between two successive fronts $dt = 2$ ms. (*b*) Flame-front evolution given by pole dynamics starting from two isolated pairs of poles. Time between two successive fronts $dt = 2$ ms. (*c*) Evolution of the squared non-dimensional distance between the two crests in the course of time. The evolution observed on experimental flame (black circles) is compared with the one given by pole dynamics given by (3.4) (red squares) and to the theoretical law (3.9) (dashed line). Here, the σ_M and k_c values are those obtained in § 3.1.

domain considered and setting the following appropriate non-dimensional variables

$$\left.\begin{aligned}
\tau &= \frac{8\pi\sigma_M}{\Lambda k_c}t, \\
X &= \frac{2\pi}{\Lambda}x, \\
\Phi &= \frac{u_A k_c \pi}{2\Lambda\sigma_M}\phi.
\end{aligned}\right\} \qquad (3.10)$$

Equation (3.1) is reduced to a one parameter equation

$$\Phi_\tau + \tfrac{1}{2}\Phi_X^2 = \nu\Phi_{XX} + I(\Phi, X), \qquad (3.11)$$

where the control parameter $1/\nu = k_c/K$ corresponds to the ratio of the width of the domain to the shortest unstable wavelength. Commonly called the unstable modes number, this parameter stands for the only non-dimensional number governing the flame dynamics. Indeed, both experimental studies (Markstein 1949; Istratov & Librovich 1969; Groff 1982; Gostintsev, Istratov & Shulenin 1989; Jomaas *et al.* 2007), and numerical experiments, either in the MS framework (Michelson & Sivashinsky 1982; Thual *et al.* 1985; Gutman & Sivashinsky 1990; Filyand, Sivashinsky & Frankel 1994; Joulin & Sivashinsky 1994), or using a fully nonlinear model (Rastigejev & Matalon 2006*a*), or direct numerical simulation (Yu *et al.* 2015), have reported a strongly dependent dynamics on this $1/\nu$ parameter. For small domains (large ν), (considering periodic boundary conditions) the dynamics always leads to a steady single crest configuration (sometimes double crest configuration for Neumann boundary conditions) whereas for larger domains, as the cells become wider, one can observe secondary wrinkles permanently appearing on the primary structures. This behaviour is in contrast with the dynamics described by (3.4), which always leads to a steady state, whatever the size of the domain (Thual *et al.* 1985; Joulin & Sivashinsky 1994; Rahibe *et al.* 1995). The differences observed between the dynamics described by

(3.1) and the one described by (3.4) for large domains, is indeed quite surprising. As first proposed by Joulin (1989), the new crest creations actually depend on the background noise (numerical noise, flow perturbations). Indeed, as first shown by Thual *et al.* (1985), the steady monocoalescent solution is the strongest attractor of (3.4) and any initial condition tends to this N_{opt} poles pile solution (Thual–Frisch–Hénon (TFH) solution). This solution is such that $2N_{opt} - 1 < 1/\nu < 2N_{opt} + 1$ (where N_{opt} is called the optimal pole number), extra poles are repealed to infinity. However, even if the TFH solution is the only stable one for both (3.1) and (3.4) (Vaynblat & Matalon 2000*a,b*), the number of equilibrium solutions is growing faster than linearly with $1/\nu$, leading rapidly to a large number of solutions (Denet 2006). The external noise, which is responsible for the permanent addition of new poles (Joulin 1988; Kupervasser, Olami & Procaccia 1996; Olami *et al.* 1997), may cause the system to permanently jump from one solution to another if poles are introduced close enough to the real axis (Denet 2006). Moreover, this unsteady behaviour can be explained without invoking nonlinear mechanisms, because of the existence of transient growth phenomena (Karlin 2002, 2004) not taken into account in the modal analysis carried out by Vaynblat & Matalon (2000*a*) and making the TFH solution an unstable equilibrium for (3.1). To be physically relevant for large-scale flames, it is thus necessary to add a stochastic forcing term in (3.1) to mimic the noise experienced by the flame front (Cambray & Joulin 1992; Cambray *et al.* 1994; Creta *et al.* 2011). From the pole decomposition standpoint, as said before, the external perturbations act as a stochastic source of new poles (Joulin 1988; Kupervasser *et al.* 1996; Olami *et al.* 1997). But until now the new poles are introduced in a completely artificial manner, and how to determine the probability function of adding a new pole at a certain location in the complex plane remains an open question. Despite this effect, in the following section we will show that the flame propagation observed in our experiments can be treated as a deterministic process for some time of evolution, and that the dynamics described by (3.4) is then experimentally relevant.

3.7. *Initial forced pole solution*

In a recent paper (Almarcha *et al.* 2018), by being able to fit the (3.3) solution on a front extracted from experiments with a small number of poles, we have already shown that pole solutions can be relevant regarding real flames. The present section is another step forward and comes with the aim of characterizing the repeatability of the experiments in order to extract a typical time beyond which the flame dynamics can no longer be described as a purely deterministic pole dynamics. In Al Sarraf *et al.* (2018*a*) and in § 3.1 the flame was initially forced with a sinusoidal profile, with the aim of selecting a specific mode and measure its growth rate. In order to study the nonlinear dynamics, the flame is now initially forced with a plate machined following a pole solution profile. For this purpose, a front shape is computed from (3.3) with a set of 16 poles arbitrarily placed in the complex plane and is machined on a plate (see figure 10).The obtained plate is then placed on the top of the burner (figure 4), in order to select this shape as an initial condition for the flame front. As in previous experiments, when the flow is stopped, the flame first enters into the Hele-Shaw burner as a flat front and is then rapidly destabilized taking the shape selected by the plate edge. As can be seen in figure 11, the selected pattern is clearly recognizable during the early time of evolution. It shows that by selecting the appropriate perturbation, it is possible to introduce some poles at desired Re(z) in the system. The imaginary parts of poles are initially quite large (the flame front is flat in the first instants) and are rapidly attracted toward the real axis, leading to the initially forced pattern. In the present case the flame just missed the last crest on the right (see figure 11). This could be due to the fact
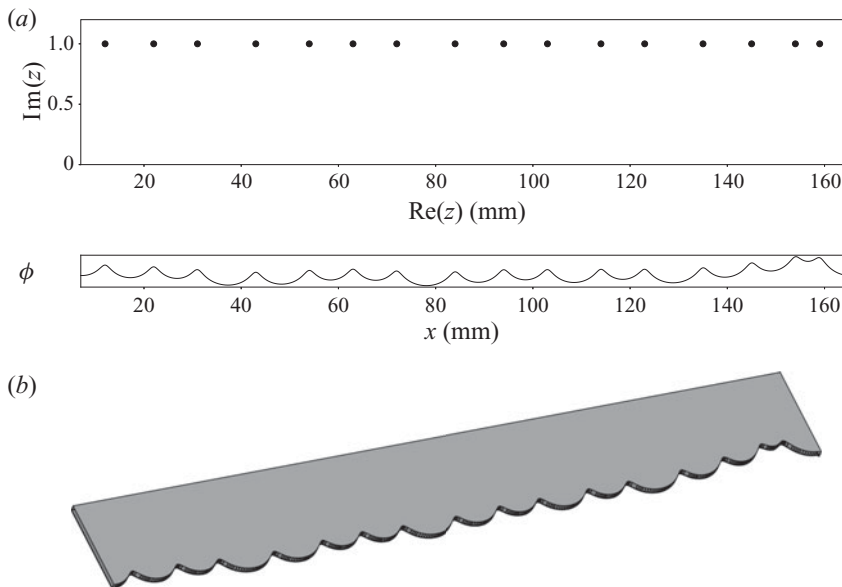
FIGURE 10. (*a*) Set of poles (only upper half of the complex plane is displayed) and the corresponding front shape described by (3.3). (*b*) Plate obtained by laser beam machining from the front shape described above. This plate is used to print initial perturbations on the front.
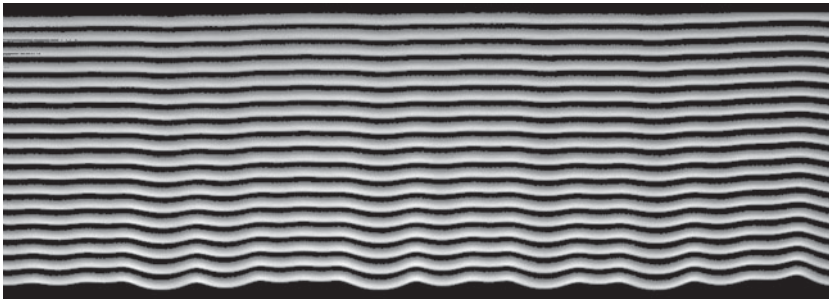

FIGURE 11. Successive fronts obtained in the first instant of propagation. Starting from a flat front, the flame is rapidly destabilized, taking the shape selected by the plate. On the last front the imposed pattern is clearly recognizable. (Fronts have been artificially shifted to distinguish each time of evolution. Time between each front $dt = 2$ ms.)

that the last two poles on the right of the plate are probably too close to each other and have merged before being attracted enough toward the real axis. However, thanks to this experimental procedure, we demonstrate that it is possible to impose an analytical initial condition for the flame front and to study its evolution in time. It allows us to study the complex nonlinear trajectories in a controlled way and to assess their repeatability.

3.8. *Experimental repeatability*

Several experiments are repeated with the same analytical initial condition (a typical evolution of the flame is displayed in figure 17*a*). Their evolutions are compared by focusing on the crests trajectories. The analysis starts when the forced crests become visible (≈ 0.156 s after the flow has been stopped). The crest trajectories of the 15 initial
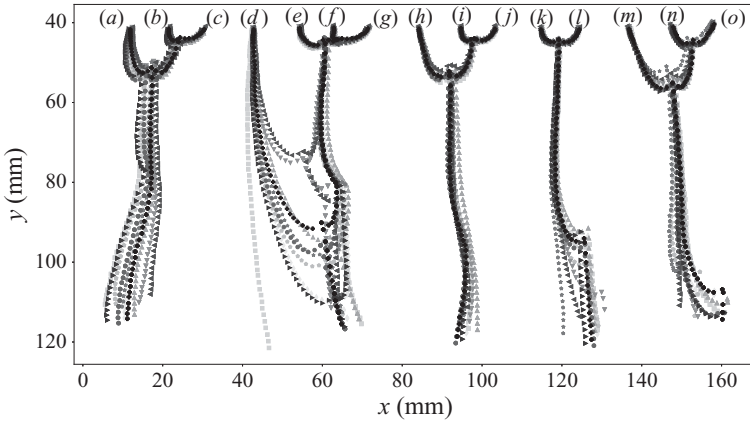
FIGURE 12. Crest trajectories comparison of the 15 initial crests for 10 different runs of the same experiment (each colour/symbol correspond to a different run). The crest trajectories go from top to bottom in 0.25 s ($\approx 10 \times t_\sigma$). Time between each point of a trajectory $dt = 4$ ms. The crests' trajectories are reproducible in the first time of propagation (upper half-part of the figure). Then new crest creations (visible by sudden directional change in the trajectories) are responsible for the scattering of trajectories $(d$–$g)$ and (k,l) in the bottom half-part of the figure.

crests are then compared for 10 different runs of this experiment (figure 12). The forcing method appears to be very efficient. The initial crest locations are almost the same for the 10 different runs. Moreover, their evolution looks extremely reproducible during a time much larger than the typical time of the instability $\approx 10 t_\sigma$. In order to quantify the similarities in trajectories, we compute the mean trajectory as

$$\left. \begin{aligned} x_{mean}^i(t) &= \frac{1}{10} \sum_{k=1}^{10} x_k^i(t), \\ y_{mean}^i(t) &= \frac{1}{10} \sum_{k=1}^{10} y_k^i(t), \end{aligned} \right\} \tag{3.12}$$

where $(x_k(t), y_k(t))$ are the coordinates of the trajectories at time t, for the run number k, and i is the trajectory index. The error on the positions $\varepsilon_k(t)$ is then computed by comparing crest positions at each run to their mean

$$\varepsilon_k(t) = \frac{1}{15} \sum_{i=(a)}^{(o)} \sqrt{\left(x_k^i(t) - x_{mean}^i(t)\right)^2 + \left(y_k^i(t) - y_{mean}^i(t)\right)^2}. \tag{3.13}$$

As shown in figure 13, the error on crest position follows an exponential growth. However, some peaks can be observed in the course of time, these local maxima in the error correspond to crest merging instants. Indeed, just before merging, the crests are moving fast and a small difference in the merging time induces a great difference in the distances. The analysis of the error growth curve allows us to quantify the repeatability of the flame dynamics by computing the Lyapunov exponent. For this purpose, each $\varepsilon_k(t)$ growth curve is non-dimensionalized by the initial error and a mean non-dimensional error
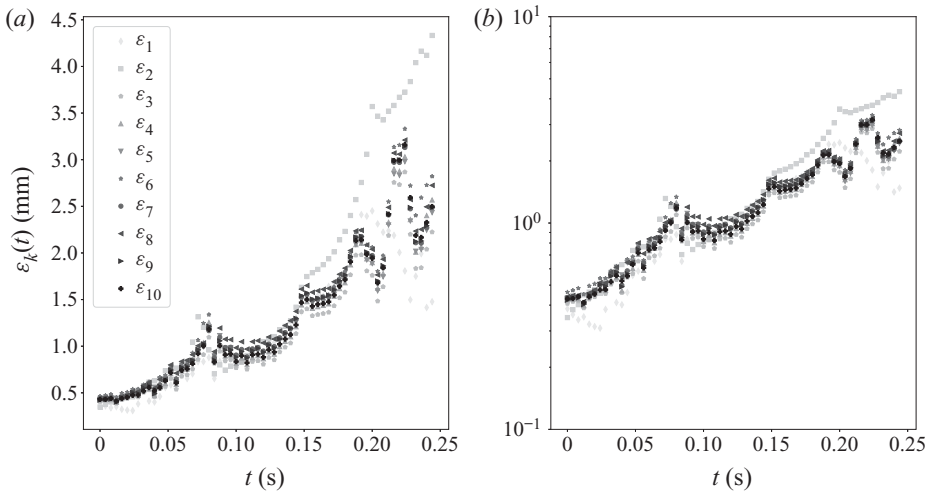
FIGURE 13. The ε evolution in the course of time for each of the 10 runs. Panel (*a*) shows lin–lin scale; (*b*) semilog scale. One can observe some peaks which correspond to the cusp merging instants. Nevertheless, despite these peaks the error follows an exponential growth.

$\tilde{\varepsilon}_{mean}$ is computed as

$$\tilde{\varepsilon}_{mean}(t) = \frac{1}{10} \sum_{k=1}^{10} \frac{\varepsilon_k(t)}{\varepsilon_k(t=0)}. \tag{3.14}$$

An exponential function $e^{\lambda t}$ is then fitted on these data. This procedure allows us to obtain the Lyapunov exponent λ (see figure 14). Here, the best fit is found to be $\lambda = 8\ \text{s}^{-1}$ corresponding to a Lyapunov horizon of $1/\lambda = 0.125$ s where λ has to be compared with $\sigma_M \approx 60\ \text{s}^{-1}$. The flame dynamics can thus be described as a purely deterministic process on times much larger than the typical Darrieus–Landau time, in the fully nonlinear regime, up to the Lyapunov horizon. Far beyond this horizon, the pattern is chaotic and external noise plays an important role. In the following, by comparing the flame evolution to the one given by pole dynamics, we will show that (3.4) is relevant to describe our experiments on times shorter than $1/\lambda$. Later in time, the flame must be described statistically.

3.9. *Comparison of analytical and experimental poles trajectories*

Equation (3.1) is an exact solution of the flame-front problem in the limit $\gamma \to 0$. This assumption can be considered as a crude one regarding a real flame (Kazakov & Liberman 2002*b*). However, as previously shown by Searby, Truffaut & Joulin (2001), (3.1) is relevant if the parameters involved in the equation are carefully chosen. Here, following the phenomenological extension of (3.1) to arbitrary values of γ proposed by Joulin & Cambray (1992), we keep the MS model in its standard form (3.1) but using the exact u_A, σ_M and k_c parameters obtained from experimental measurements.

The exact σ_M and k_c values for our experiments are those previously obtained in § 3.1. A front is then extracted by image processing from an experimental capture, at early time (0.156 s) (see figure 15). Then, following the procedure introduced in Almarcha *et al.* (2018) and providing the σ_M and k_c values determined in § 3.1, a pole solution (3.3) is fitted on the experimental front, by searching for the pole positions $z_n = \text{Re}(z_n) + i\text{Im}(z_n)$ and
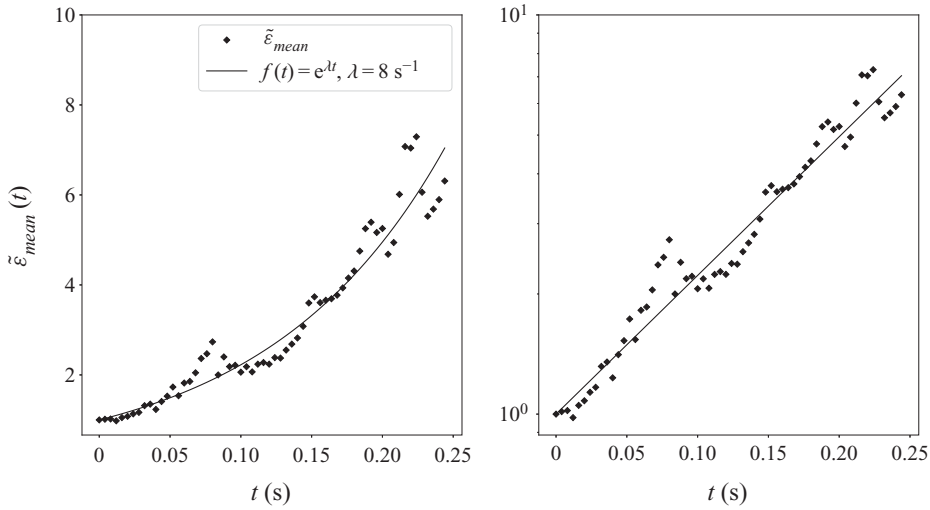
FIGURE 14. Evolution of the mean non-dimensionalized error in the course of time. An exponential is fitted on these data in order to determine the Lyapunov exponent of the system.
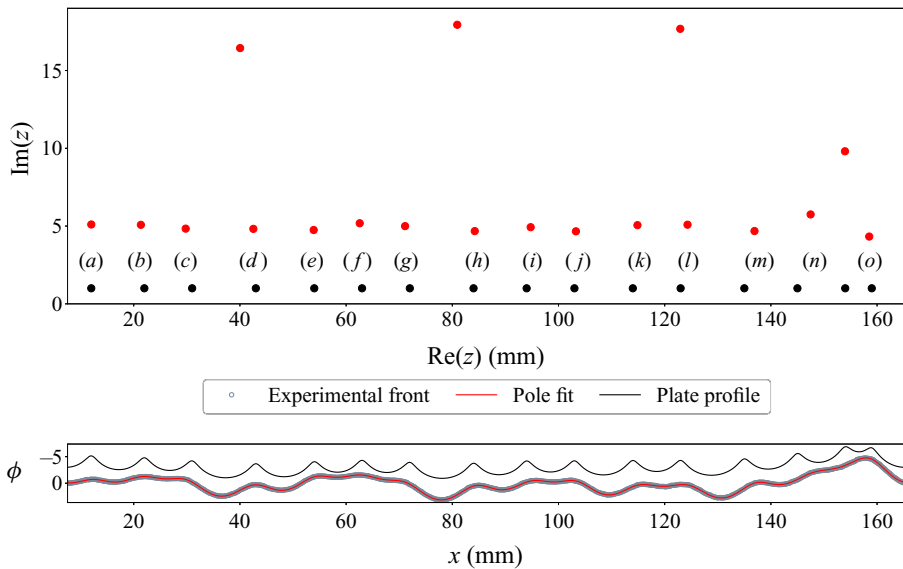

FIGURE 15. Comparison of the forcing plate profile (black line and black dots) with the experimental front (grey circles) and its best pole decomposition (red line and red dots) obtained by a Levenberg–Marquardt fitting algorithm. The amplitude has been multiplied by a factor of 5 for the experimental front and the fitted solution. The nearest poles to the real axis are responsible for crests at same abscissa on the front, whereas the further are flattening the larger cells.

the amplitude A that minimizes the error in a least square sense (see figure 15 (redline)). The first thing to note is that, although the plate profile is a 16 poles solution, we have not been able to fit the experimental front with only 16 poles. A minimum of 19 poles has been necessary to obtain the convergence of our Levenberg–Marquardt fitting algorithm. It explains the presence of three large imaginary part poles (figure 15). As they are far
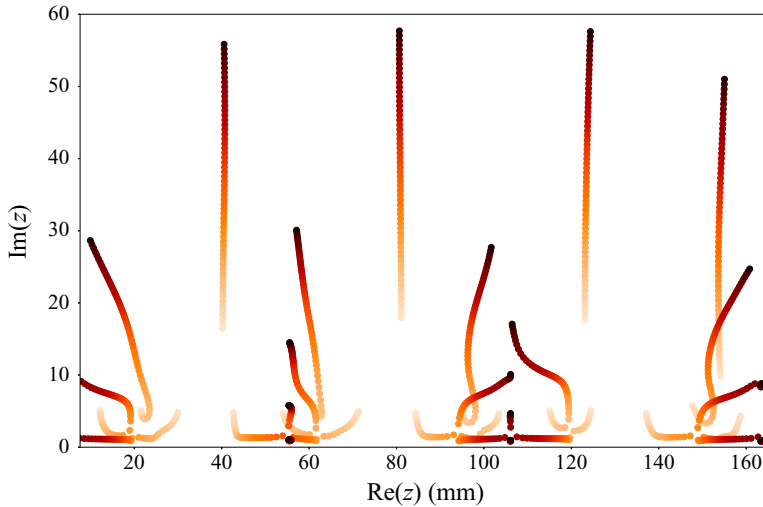
FIGURE 16. Pole trajectories (time goes from light to dark) obtained from integration of (3.4), starting from the fitted pole solution (figure 15 (red dots)). Total time evolution is 0.25 s.

from the real axis these three exceeding poles are not associated with the presence of crests but are just flattening the largest cells. Their possible influence in the dynamics will be discussed later. This solution and its corresponding poles (figure 15 (red)) are then compared with the plate profile used to force the initial condition (figure 15 (blue)). As can be seen, the $\text{Re}(z_n)$ positions of the 15 nearest poles to the real axis (figure 15 (red dots)) are almost identical to the expected poles positions (figure 15 (blue dots)). However, one can note that their imaginary parts, $\text{Im}(z_n)$, are substantially larger ($\approx 5\times$) than those associated with the plate profile. As a consequence, the profile on the plate is more cusped than the flame profile. This difference can be adjusted with the distance between the plate and the initial anchored inverted-V flame. The closer the plate, the more pronounced are the cusps in the initial flame profile. To summarize, the plate method allows us to introduce some poles at given $\text{Re}(z)$ positions but with low control on their $\text{Im}(z)$ location. Moreover, in § 3.7, we argued that the two last crests on the right-hand side of the forced solution could have merged in one (crest (o)) due to the merging of the two corresponding poles before they have been attracted toward the real axis. This statement is actually corroborated by the fitted solution, where two poles form a pile at the (o) crest position.

Since an accurate pole decomposition of the experimental front has been obtained, the dynamics described by (3.4) can now be compared with the experimental evolution. For this purpose, starting from the fitted solution (figure 15 (red dots)), the system of ordinary differential equations (3.4), is numerically integrated thanks to a fourth-order Runge–Kutta algorithm. This integration gives the pole trajectories in the complex plane (figure 16). At each instant of the evolution, the flame front is then obtained from the current position of the poles using (3.3). The resulting flame-front evolution is shown in figure 17(c). The latter is compared with the evolution given by MS pseudo differential equation (PDE) integration (3.1) (figure 17b), starting from the initial experimental front. The evolution given by the pole dynamics and the one given by MS PDE are nearly identical. This observation attests to the quality of the fit realized in figure 15. Moreover, these two evolutions obtained from the MS model agree well with the experimental one
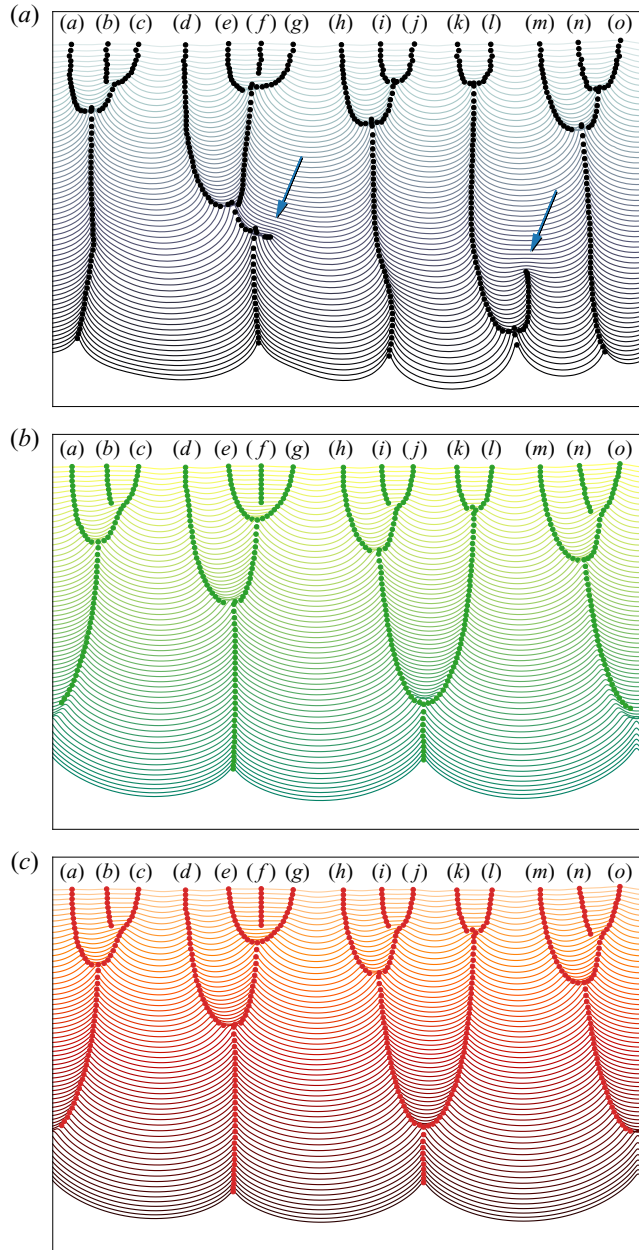
FIGURE 17. Comparison between experimental evolution of a propane–air flame $\varphi = 0.8$ and the corresponding evolution given by the MS PDE and by pole dynamics. (*a*) Typical experimental evolution obtained by forcing an initial condition using the pole profiled plate method. (*b*) Corresponding evolution given by MS PDE, starting from the initial experimental front. (*c*) Corresponding evolution given by pole dynamics, starting from the pole solution corresponding to the initial experimental front. Flame goes from top to bottom in 0.25 s. Time between each front $dt = 4$ ms.

during, approximately, the half-part of the plot ($\approx$0.125 s). This typical time corresponds to the Lyapunov horizon determined in § 3.8. Beyond this characteristic time the system loses memory of the initial condition and become unpredictable.

During the first half-part of the evolution, the 15 poles associated with crests are first attracted toward the real axis (figure 16), leading to a more cusped front (see figure 17). Then, due to the horizontal interaction, they attract each other, pilling up at same abscissas. This process is the mechanism responsible for the merging of crests observed in the experiments.

During the second half-part of the propagation, the crests trajectories described by pole dynamics are diverging from the experimental ones. This is actually due to the already mentioned issue of new cusp creation. Looking at figure 17, one can observe two crest creations (pointed out by arrows). These new cusps are responsible for the disparity in crest trajectories, observed in the previous section (see figure 12). As quoted before, these new crests may come from poles originally far from the real axis that have been attracted toward the real axis (see figure 7), or by an external forcing responsible for the injection of new poles in the system. However, if the latter is true, one can note that these new crests are appearing always in the same zone for the 10 experimental runs considered in the present paper (see figure 12). Then, if an external noise is responsible for the appearance of these new crests, it means that the flame possesses regions that are more sensitive to noise than others, otherwise new crests come from poles which were initially present. In that case, one can ask about the three exceeding poles in the fitted initial solution. We can postulate three different interpretations for their presence: (i) the pole decomposition (3.3) is a too simplistic description regarding real flames and therefore we have not been able to fit the flame with just one pole at each crest; (ii) the exceeding poles have been embedded by an external source of noise during the first instant of propagation; (iii) the plate forcing method is not accurate enough and inserted some undesirable poles. These exceeding singularities could be responsible for the formation of new crests observed in the experiments. However, to make new crests, these poles should be attracted toward the real axis and it is obviously not what is predicted by (3.4) (see figure 16). The additional poles are rapidly spurned to $\pm i\infty$, and never lead to the generation of new crests (see evolution on figure 17). Indeed for the present case, $\Lambda/\lambda_c = 1/\nu = 21.4$, corresponding to an optimal number of poles of $N_{opt} = 11$ (see Thual *et al.* 1985). Therefore, initially, there are eight poles in excess that have to be pushed away from the real axis. This explains why these poles are not attracted toward the real axis. Nevertheless, some key features such as gravity or heat loss effects are not taken into account in the MS model and may be responsible for slight modifications in the pole dynamics, eventually leading to the attraction of exceeding poles toward the real axis. Yet, the latter remark is purely speculative as until now no pole description that takes gravity effects into account has been obtained.

As presumed, the generation of new crest is a key component in the flame dynamics and is responsible for the non-repeatability of the crest trajectories, and thus to the failure of a pole dynamics forecast after some time of evolution.

4. Late-time evolution

4.1. *Expected cell size distribution*

As shown in the previous section, the deterministic stage of large-scale flames ends after the Lyapunov horizon $1/\lambda$, when new crests creations arise. The dynamics is then sensitive to external forcing (e.g. thermal noise, residual turbulence or vibrations) or
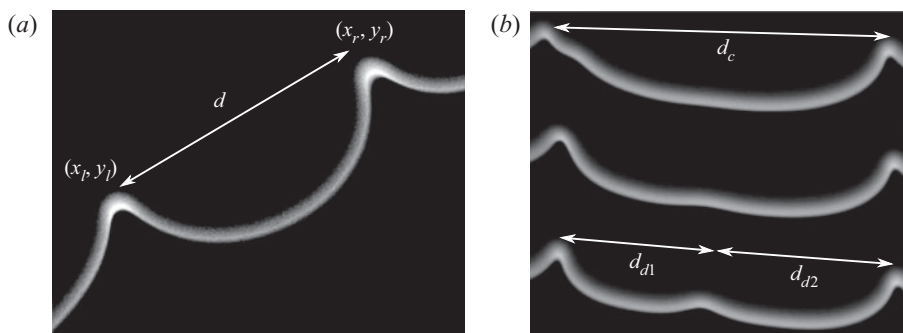
FIGURE 18. (*a*) Typical measure of a cell on a propane–air flame $\varphi = 0.8$. Field of view: 30 mm. (*b*) Cell of size d_c giving birth to two daughter cells of size d_{d1} and d_{d2} by splitting.

to self-generated large-scale perturbations, and must be studied as a stochastic process. As explained in Cambray *et al.* (1994), when a cell gets sufficiently large, a new crest appears and splits the cell in two. As a result, instead of continuously growing up to the size of the domain of propagation, the mean cell size saturates to a stationary value that decreases when the forcing noise intensity increases. Moreover, when changing the properties of the reacting gas, the mean cell size is also expected to vary. We focus here on the distribution of the cells sizes around the mean. As the problem is composed of two competing phenomena, the new crests generation that dominates on large cells, and the crest coalescence that dominates at small scale, we can expect a stationary distribution as demonstrated in Escobedo, Mischler & Ricard (2005). Assuming that the cells split at random, the tail of the distribution (for large cells where fragmentation dominates) is expected to have an exponential decay

$$p\,(d \gg \langle d \rangle) \propto \mathrm{e}^{-d}. \tag{4.1}$$

At small scales, the coalescence of cusps dominates and is described by (3.9) so that the probability of occurrence of each scale is proportional to its lifetime during the kinematic coalescence process. This lifetime is inversely proportional to the rate of variation of the size in time during coalescence, namely $\mathrm{d}d/\mathrm{d}t = -32\sigma_M/k_c^2 d$ according to (3.9), so that

$$p\,(d \ll \langle d \rangle) \propto \frac{k_c^2}{32\sigma_M}d. \tag{4.2}$$

The whole distribution is expected to respect the two conditions, (4.1) and (4.2), and therefore to follow a gamma distribution (Villermaux & Duplat 2003) as introduced in Almarcha *et al.* (2018),

$$p\left(x = \frac{d}{\langle d \rangle}\right) = \frac{4}{\Gamma(2)}x\,\mathrm{e}^{-2x}. \tag{4.3}$$

In order to compare this theoretical prediction for the cell size distribution, we carried out both numerical and laboratory experiments. Both for the fronts extracted from numerical simulations and those extracted from experimental images, crest positions are localized by way of a continuous wavelet transform method (Du, Kibbe & Lin 2006). The cell size distribution is then computed by measuring the distance between each crest, $d = \sqrt{(x_r - x_l)^2 + (y_r - y_l)^2}$ (see figure 18).

4.1.1. *Numerical experiments*

The numerical experiments are performed in the MS framework to allow large-scale flame simulations for a limited cost. The non-dimensional Sivashinsky equation (3.11) is integrated by way of Fourier pseudospectral method (Giada, Giacometti & Rossi 2002), starting from a flat front with small amplitude white noise and periodic boundary conditions. The integration in time is performed by way of the finite difference method with a semi-implicit scheme (forward/backward Euler). The simulations are carried out over a large time $t \gg t_\sigma$ in order to have a large statistical sampling to compute the cell size distribution. As stated before, the emergence of new crests are related to a sensitivity to external perturbative noise which can be round-off errors, for instance. In order to test the influence of the noise intensity on the cell size distribution, we integrated the following forced MS equation (pseudospectral method domain of width $\Lambda = 2\pi$ with 2048 Fourier modes and time step $\Delta t = 10^{-5}$):

$$\Phi_\tau + \tfrac{1}{2}\Phi_X^2 = \nu\Phi_{XX} + I(\Phi, X) + \eta(x, t), \tag{4.4}$$

with $\eta(x, t)$ a Gaussian white noise probability density function

$$f(\eta) = \frac{1}{s\sqrt{2\pi}} \exp\left(-\frac{\eta^2}{2s^2}\right). \tag{4.5}$$

The cell size distribution is then computed following the procedure described earlier, from simulations with different noise intensities. The corresponding results are plotted in figure 19. One can see that even if the noise intensity has a strong influence on the mean cell size, the non-dimensional distribution is not affected and is perfectly matching the expected law (4.3)

4.1.2. *Experiments in the Hele-Shaw burner*

The experiments are performed in the apparatus described in § 2 using the experimental procedure described in § 2.1. The high-speed Photron camera (field of view 50 cm × 50 cm) is placed between $y = 75$ and $y = 125$ cm under the top of the burner, in order to be far from the first instants of propagation and reach fully developed dynamics, and to be far from the closed end of the burner (to avoid confinement effects on the unburned gas side). The experiments are performed with propane–air mixtures for a large range of equivalence ratios ($0.8 < \varphi < 1.3$). For each mixture the experiments are repeated approximately 30 times in order to have a large statistical sample ($\approx 10^4$ occurrences for each mixture). Moreover, the acquisition frame rate $1/t_{frame}$ of the high-speed camera is adjusted in order to be large enough with respect to the observed dynamics $t_{frame} \approx 0.5t_\sigma$. The flame fronts are extracted from these images using the procedure described in § 2.4.

The results obtained numerically and experimentally are presented in figure 20. First, by comparing with growth rate measurements in Al Sarraf *et al.* (2018*a*) and Al Sarraf *et al.* (2018*b*), one can note that, as first observed by Markstein (1949), the mean cell size $\langle d \rangle$ is much larger than the most unstable wavelength λ_{max} ($\langle d \rangle \approx 5\lambda_{max}$) predicted by the linear theory. Furthermore, due to thermodiffusive properties of the C3H8–air mixture, $\langle d \rangle$ is noticeably decreasing when the equivalence ratio is increased (figure 20*a*–*c*). However, despite the variations of the mean size with the equivalence ratio, all the cell size distributions collapse on a same curve when non-dimensionalized by the mean cell size $\langle d \rangle$ (see figure 20*d*–*f*). This self-similar property is a common feature of a Smoluchowski aggregation process (Swift & Friedlander 1964; Hidy 1965; Friedlander & Wang 1966;
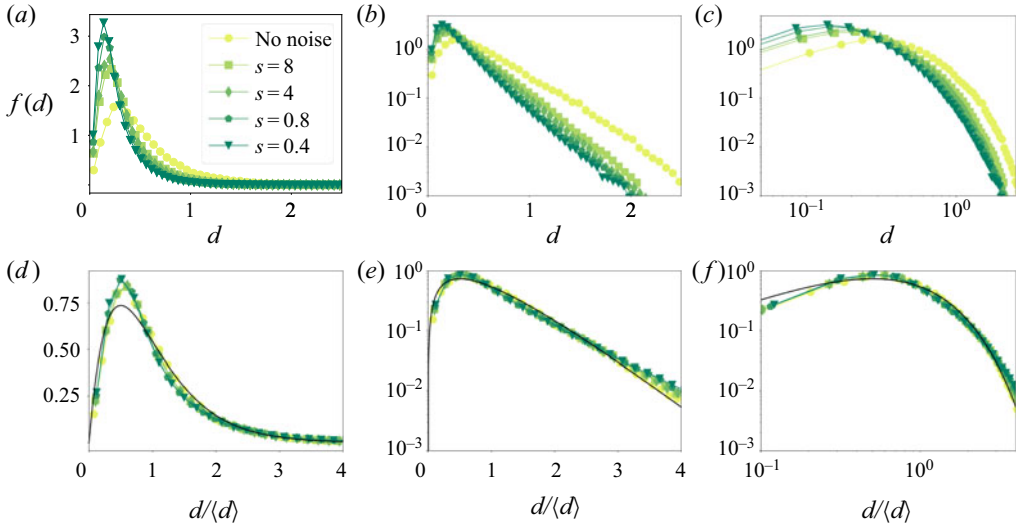
FIGURE 19. Cell size distributions computed from forced MS simulations (see (4.4)) on a domain of width $\Lambda = 2\pi$ with periodic boundary conditions and 2048 Fourier modes and time step $\Delta t = 10^{-5}$. For all the simulations only the noise intensity is varied, the unstable mode number is fixed to $1/\nu = 200$. (*a*) Dimensional cell size distribution lin–lin scale. (*b*) Dimensional cell size distribution semilog scale. (*c*) Dimensional cell size distribution log–log scale. (*d*) Non-dimensional cell size distribution lin–lin scale. (*e*) Non-dimensional cell size distribution semilog scale. (*f*) Non-dimensional cell size distribution log–log scale.

Fournier & Laurençot 2005). However, although the experimental distributions all collapse on the same curve, one can note a significant lack of large cells regarding the cell size distribution obtained numerically and the theoretical distribution given by (4.3). As this discrepancy concerns lengths much larger than the mean, we can expect that the splitting mechanism is different in the numerics and in the experiments. We can expect that the experimental large-scale cells are relatively more prone to split than the numerical ones. In order to confirm this tendency, we identify the new crest appearance and measure the size d_c just before cells split (see figure 18), either from experimental or numerical fronts. The distribution of the cells that split is reported in figure 21(*b*). Of course, such a distribution is linked to the probability of presence of each cell in figure 21(*a*). In particular, few cells are splitting for sizes $d/\langle d \rangle > 3$ mainly because very few of these big cells are present along the flame front. In order to determine the natural tendency for each cell to break depending on their size, we divide the distribution in figure 21(*b*) by the distribution in figure 21(*a*) to obtain figure 21(*c*). The result is related to the lifetime expectation or conversely, to the probability per unit time for a specific cell to break when it is of size d, which according to Bayes' theorem (Bayes, Price & Canton 1763; Laplace 1774) is given by

$$P_d(c) = \frac{P_c(d)P(c)}{P(d)}, \tag{4.6}$$

with $P_c(x = d \in [a, b]) = \int_a^b f_c(x)\,dx$ the probability that a cell splits given it is of size d, $P(c)$ the probability of splitting and $P(x = d \in [a, b]) = \int_a^b f(x)\,dx$ the probability for a
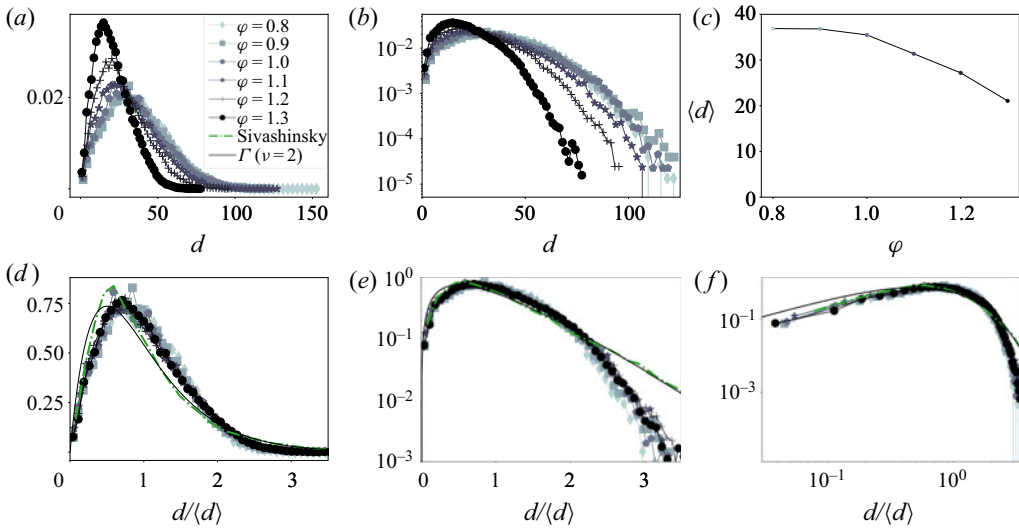
FIGURE 20. Experimental cell size distributions for propane–air flame at different equivalence ratio compared with theoretical and numerical ones. (*a*) Dimensional cell size distribution lin–lin scale. (*b*) Dimensional cell size distribution semilog scale. (*c*) Mean cell size evolution with equivalence ratio. (*d*) Non-dimensional cell size distribution lin–lin scale. (*e*) Non-dimensional cell size distribution semilog scale. (*f*) Non-dimensional cell size distribution log–log scale.
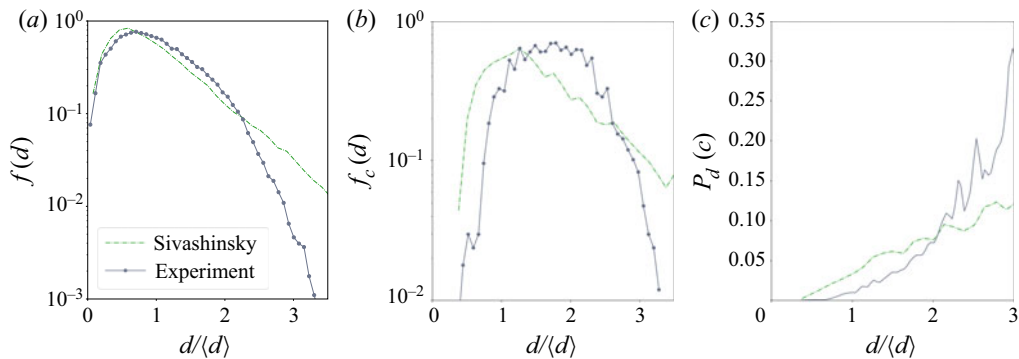

FIGURE 21. Cell splitting statistics. (*a*) Non-dimensional cell size probability density function for experimental and numerical (MS) fronts. (*b*) Probability density function of cell size which splits. (*c*) Probability to split per time unit for a given cell of size d, as a function of d.

cell to be d in size, giving

$$\Leftrightarrow P_d(c) = \frac{f_c(d)P(c)}{f(d)}. \tag{4.7}$$

This quantity is displayed in the last plot of figure 21. The difference, between experimental and numerical results, in the way external perturbations affect cell splitting is now made very clear. Indeed, for Sivashinsky simulations, the probability of splitting for a given cell of size d exhibits a linear growth with d, which is compatible with a probability of breaking, per unit length, which is constant. This particular property is the signature

of a random splitting mechanism along the flame front. Conversely, for experimental flames, the probability grows faster than linearly with cell size, showing that a cell is more sensitive to noise when it becomes larger. This characteristic reveals the presence of a mechanism, acting specifically on large cells, that breaks the random splitting hypothesis. A probable candidate is the gravity field that may flatten the largest cells by a buoyancy effect and make them more sensitive to noise. Another candidate is the heat loss on the glass plates behind the flame that may decrease the Darrieus–Landau effect for large cells and especially cells much larger than the cooling length. The analysis of these effects shall be addressed in a forthcoming study.

5. Conclusion

For nearly one hundred and fifty years premixed flames have been known to exhibit a cellular pattern. Despite many attempts to characterize theoretically and experimentally their evolution and scalings, there was no robust and complete mechanism to explain the properties and the evolution of such a pattern. As the combustion process involves a complex reactive fluid dynamics with strong density gradients, the major part of the studies has tried to tackle the question with the help of simplified models, by considering the flame as a gasdynamic discontinuity, between two flows of different densities (Frankel & Sivashinsky 1982; Matalon & Matkowsky 1982; Pelce & Clavin 1982). In this framework much effort has been made to obtain an equation for this interface in a closed form (i.e. in a form involving only quantities defined on the flame front) (Sivashinsky 1977; Sivashinsky & Clavin 1987; Joulin & Cambray 1992; Bychkov 1998; Bychkov & Kleev 1999; Bychkov, Kovalev & Liberman 1999; Kazakov & Liberman 2002*a,b*; Kazakov 2005*a,b*; Joulin, El-Rabii & Kazakov 2008; El-Rabii, Joulin & Kazakov 2010; Assier & Wu 2014). However, to obtain such an equation is an extremely intricate mathematical problem because it requires solving the whole flow both ahead and behind the flame front. Therefore, to obtain such an equation generally requires some strong assumptions. One of them consists in developing all the quantities involved in the problem in the small expansion limit. Despite such a crude assumption, the obtained equation was already known for years to reproduce, qualitatively well, the essential features of flame dynamics observed in experiments. Moreover, the obtained nonlinear equation admits pole solutions, which make the dynamics analytically tractable. However, until now there was no experimental evidence of its validity on fully developed nonlinear stages. In most experimental facilities used previously the flame front consisted of a three-dimensional reaction sheet, and the analysis of the front properties is an extremely difficult task.

In this study we use a simplified apparatus that constrains the dynamics to two dimensions only, and despite the heat and momentum losses induced by the confined geometry, the flame dynamics remains of the same nature as in three-dimensional geometries. Thus, the flame-front analysis is greatly simplified, and its description is more accurate. For instance, the experimental tracking of two crests merging has been successfully compared with an expected analytical model of d^2 law.

In addition, we used an improved version of a technique recently introduced by Al Sarraf *et al.* (2018*a*) where a forcing plate at the top of the burner creates a wrinkling of the flame front. Using a plate machined by laser-cutting, we are now able to print perturbations on the flame front, and to impose precisely the position of the crests that will develop. Thanks to this method, the experimental repeatability has been studied, by performing the experiments several times from the same forced initial condition. The largest Lyapunov exponent of the system has been computed by analysing these experiments. It allows us to

identify the characteristic time (the Lyapunov horizon), beyond which the flame dynamics is no longer predictable. When the initially imposed perturbation is an analytic solution of the MS model (i.e. a pole solution), we demonstrated that it is possible to impose the whole analytic nonlinear trajectory to the flame front for times as late as a decade further than the linear growth time. It is a great demonstration of the astonishing accuracy of the pole description.

Later in time the external perturbations play an important role. Moreover, the front is prone to develop large slopes, therefore the MS model is valid locally only. Nevertheless, we have highlighted that for the statistically stationary late-time dynamics, the elementary pole attraction is still ruling the pattern through an aggregation process combined with a fragmentation process. This fragmentation is inducing the large cells statistic decay. In the case of the MS equation forced with additive white noise at random, a gamma distribution was obtained whatever the noise intensity. In the experiments, a faster decrease of the distribution was obtained, expressing that large cells have an enhanced tendency to break, certainly due to gravity or heat loss effects.

Finally, a perspective opened by this study is to extend the present work to three-dimensional flames. Here again, as the analysis of three-dimensional experimental flames is intricate, numerics seems to be the best way to achieve it. In the MS framework, it has been shown that because of the nature of the nonlinear term involved in the MS PDE, the dynamics in x and y directions are completely independent (Denet 2007), therefore the analysis carried out in this paper is still valid. However, the x and y dynamics should be coupled for finite γ values. To investigate this question, the recent extension of the fully nonlinear model introduced in Rastigejev & Matalon (2006*b*) to three-dimensional geometry (Patyal & Matalon 2018) is really promising for large-scale flame dynamics analysis.

Acknowledgements

Declaration of interests

The authors report no conflict of interest.

REFERENCES

AL SARRAF, E., ALMARCHA, C., QUINARD, J., RADISSON, B., DENET, B. 2018*a* Quantitative analysis of flame instabilities in a Hele-Shaw burner. *Flow Turbul. Combust.* **101** (3), 851–868.

AL SARRAF, E., ALMARCHA, C., QUINARD, J., RADISSON, B., DENET, B., GARCIA-YBARRA, P. 2018*b* Darrieus–Landau instability and Markstein numbers of premixed flames in a Hele-Shaw cell. *Proc. Combust. Inst.* **37** (2), 1783–1789.

ALMARCHA, C., DENET, B. & QUINARD, J. 2015 Premixed flames propagating freely in tubes. *Combust. Flame* **162** (4), 1225–1233.

ALMARCHA, C., RADISSON, B., AL SARRAF, E., VILLERMAUX, E., DENET, B. & QUINARD, J. 2018 Interface dynamics, pole trajectories, and cell size statistics. *Phys. Rev.* E **98** (3), 030202.

ALTANTZIS, C., FROUZAKIS, C. E., TOMBOULIDES, A. G., MATALON, M. & BOULOUCHOS, K. 2012 Hydrodynamic and thermodiffusive instability effects on the evolution of laminar planar lean premixed hydrogen flames. *J. Fluid Mech.* **700**, 329–361.

ASSIER, R. C. & WU, X. 2014 Linear and weakly nonlinear instability of a premixed curved flame under the influence of its spontaneous acoustic field. *J. Fluid Mech.* **758**, 180–220.

BAYES, T., PRICE, R. & CANTON, J. 1763 An essay towards solving a problem in the doctrine of chances.

BESSIS, D. & FOURNIER, J. D. 1984 Pole condensation and the Riemann surface associated with a shock in Burgers' equation. *J. Phys. Lett.* **45** (17), 833–841.

BRADLEY, D. 1999 Instabilities and flame speeds in large-scale premixed gaseous explosions. *Phil. Trans. R. Soc. Lond.* A **357** (1764), 3567–3581.

BYCHKOV, V. & KLEEV, A. 1999 The nonlinear equation for curved flames applied to the problem of flames in cylindrical tubes. *Phys. Fluids* **11** (7), 1890–1895.

BYCHKOV, V. V. 1998 Nonlinear equation for a curved stationary flame and the flame velocity. *Phys. Fluids* **10** (8), 2091–2098.

BYCHKOV, V. V., KOVALEV, K. A. & LIBERMAN, M. A. 1999 Nonlinear equation for curved nonstationary flames and flame stability. *Phys. Rev.* E **60** (3), 2897–2911.

CAMBRAY, P., JOULAIN, K. & JOULIN, G. 1994 Mean evolution of wrinkle wavelengths in a model of weakly-turbulent premixed flame. *Combust. Sci. Technol.* **103** (1–6), 265–282.

CAMBRAY, P. & JOULIN, G. 1992 On moderately-forced premixed flames. *Symp. Combust.* **24** (1), 61–67.

CLANET, C. & SEARBY, G. 1998 First experimental study of the Darrieus–Landau instability. *Phys. Rev. Lett.* **80** (17), 3867–3870.

CRETA, F., FOGLA, N. & MATALON, M. 2011 Turbulent propagation of premixed flames in the presence of Darrieus–Landau instability. *Combust. Theor. Model.* **15** (2), 267–298.

CRETA, F. & MATALON, M. 2011 Strain rate effects on the nonlinear development of hydrodynamically unstable flames. *Proc. Combust. Inst.* **33** (1), 1087–1094.

DARRIEUS, G. 1938 Propagation d'un front de flamme. *La Technique Moderne* **30**, 18.

DENET, B. 2006 Stationary solutions and Neumann boundary conditions in the Sivashinsky equation. *Phys. Rev.* E **74** (3), 036303.

DENET, B. 2007 Sivashinsky equation in a rectangular domain. *Phys. Rev.* E **75** (4), 046310.

DU, P., KIBBE, W. A. & LIN, S. M. 2006 Improved peak detection in mass spectrum by incorporating continuous wavelet transform-based pattern matching. *Bioinformatics* **22** (17), 2059–2065.

EL-RABII, H., JOULIN, G. & KAZAKOV, K. A. 2010 Stability analysis of confined V-shaped flames in high-velocity streams. *Phys. Rev.* E **81** (6), 066312.

ESCOBEDO, M., MISCHLER, S. & RICARD, M. R. 2005 On self-similarity and stationary problem for fragmentation and coagulation models. *Ann. Inst. Henri Poincaré* **22**, 99–125.

FILYAND, L., SIVASHINSKY, G. I. & FRANKEL, M. L. 1994 On self-acceleration of outward propagating wrinkled flames. *Physica* D **72** (1–2), 110–118.

FOURNIER, N. & LAURENÇOT, P. 2005 Existence of self-similar solutions to Smoluchowski's coagulation equation. *Commun. Math. Phys.* **256** (3), 589–609.

FRANKEL, M. L. & SIVASHINSKY, G. I. 1982 The effect of viscosity on hydrodynamic stability of a plane flame front. *Combust. Sci. Technol.* **29** (3–6), 207–224.

FRIEDLANDER, S. K. & WANG, C. S. 1966 The self-preserving particle size distribution for coagulation by Brownian motion. *J. Colloid Interface Sci.* **22** (2), 126–132.

GIADA, L., GIACOMETTI, A. & ROSSI, M. 2002 Pseudospectral method for the Kardar-Parisi-Zhang equation. *Phys. Rev.* E **65** (3), 036134.

GOSTINTSEV, Y. A., ISTRATOV, A. G. & SHULENIN, Y. V. 1989 Self-similar propagation of a free turbulent flame in mixed gas mixtures. *Combust. Explos. Shock Waves* **24** (5), 563–569.

GROFF, E. G. 1982 The cellular nature of confined spherical propane-air flames. *Combust. Flame* **48**, 51–62.

GUTKOWSKI, A. & JAROSIŃSKI, J. 2009 Flame propagation in narrow channels and mechanism of its quenching. In *Combustion Phenomena, Selected Mechanisms of Flame Formation, Propagation and Extinction* (ed. J. Jarosinski & B. Veyssiere), pp. 102–110. CRC Press.

GUTMAN, S. & SIVASHINSKY, G. I. 1990 The cellular nature of hydrodynamic flame instability. *Physica* D **43** (1), 129–139.

HIDY, G. M. 1965 On the theory of the coagulation of noninteracting particles in Brownian motion. *J. Colloid Sci.* **20** (2), 123–144.

ISTRATOV, A. G. & LIBROVICH, V. V. 1969 Stability of flames. *Tech. Rep.* Army Foreign Science and Technology Center.

JANG, H. J., JANG, G. M. & KIM, N. I. 2018 Unsteady propagation of premixed methane/propane flames in a mesoscale disk burner of variable-gaps. *Proc. Combust. Inst.* **37** (2), 1861–1868.

JOMAAS, G., LAW, C. K. & BECHTOLD, J. K. 2007 On transition to cellularity in expanding spherical flames. *J. Fluid Mech.* **583**, 1–26.

JOULIN, G. 1988 On a model for the response of unstable premixed flames to turbulence. *Combust. Sci. Technol.* **60** (1–3), 1–5.

JOULIN, G. 1989 On the hydrodynamic stability of curved premixed flames. *J. Phys.* **50** (9), 1069–1082.

JOULIN, G. & CAMBRAY, P. 1992 On a tentative, approximate evolution equation for markedly wrinkled premixed flames. *Combust. Sci. Technol.* **81** (4–6), 243–256.

JOULIN, G., EL-RABII, H. & KAZAKOV, K. A. 2008 On-shell description of unsteady flames. *J. Fluid Mech.* **608**, 217–242.

JOULIN, G. & SIVASHINSKY, G. 1994 Influence of momentum and heat losses on the large-scale stability of Quasi-2D premixed flames. *Combust. Sci. Technol.* **98** (1–3), 11–23.

KARLIN, V. 2002 Cellular flames may exhibit a non-modal transient instability. *Proc. Combust. Inst.* **29** (2), 1537–1542.

KARLIN, V. 2004 Estimation of the linear transient growth of perturbations of cellular flames. *Math. Models Meth. Appl. Sci.* **14** (8), 1191–1210.

KARLOVITZ, B., DENNISTON, D. W. & WELLS, F. E. 1951 Investigation of turbulent flames. *J. Chem. Phys.* **19** (5), 541–547.

KAZAKOV, K. A. 2005*a* Exact equation for curved stationary flames with arbitrary gas expansion. *Phys. Rev. Lett.* **94** (9), 094501.

KAZAKOV, K. A. 2005*b* On-shell description of stationary flames. *Phys. Fluids* **17** (3), 032107.

KAZAKOV, K. A. & LIBERMAN, M. A. 2002*a* Effect of vorticity production on the structure and velocity of curved flames. *Phys. Rev. Lett.* **88** (6), 064502.

KAZAKOV, K. A. & LIBERMAN, M. A. 2002*b* Nonlinear equation for curved stationary flames. *Phys. Fluids* **14** (3), 1166–1181.

KUPERVASSER, O., OLAMI, Z. & PROCACCIA, I. 1996 Geometry of developing flame fronts: analysis with pole decomposition. *Phys. Rev. Lett.* **76** (1), 146.

LANDAU, L. D. 1944 On the theory of slow combustion. *Acta Phys.* **19**, 77–85.

LANDAU, L. D. & LIFSHITZ, E. M. 1959 *Fluid Mechanics*. Pergamon.

LAPLACE, P.-S. 1774 Mémoire sur la probabilité des causes par les évènements. *Memoires de Mathematiques et Physique, Presentés à l'Académie Royale des Sciences* **66**, 621–656.

LAYZER, D. 1955 On the instability of superposed fluids in a gravitational field. *Astrophys. J.* **122**, 1.

LEE, Y. C. & CHEN, H. H. 1982 Nonlinear dynamical models of plasma turbulence. *Phys. Scr.* **T2A**, 41–47.

MALLARD, E. & LE CHATELIER, H. 1883 *Recherches Expérimentales et Théoriques Sur La Combustion Des Mélanges Gazeux Explosives*. H. Dunod et E. Pinat.

MANTON, J., VON ELBE, G. & LEWIS, B. 1952 Nonisotropic propagation of combustion waves in explosive gas mixtures and the development of cellular flames. *J. Chem. Phys.* **20** (1), 153–157.

MARKSTEIN, G. H. 1949 Cell structure of propane flames burning in tubes. *J. Chem. Phys.* **17** (4), 428–429.

MARKSTEIN, G. H. 1951 Experimental and theoretical studies of flame-front stability. *J. Aeronaut. Sci.* **18** (3), 199–209.

MATALON, M. & MATKOWSKY, B. J. 1982 Flames as gasdynamic discontinuities. *J. Fluid Mech.* **124** (1), 239–259.

MEUNIER, P. & LEWEKE, T. 2003 Analysis and treatment of errors due to high velocity gradients in particle image velocimetry. *Exp. Fluids* **35** (5), 408–421.

MICHELSON, D. M. & SIVASHINSKY, G. I. 1977 Nonlinear analysis of hydrodynamic instability in laminar flames–II. Numerical experiments. *Acta Astron.* **4** (11–12), 1207–1221.

MICHELSON, D. M. & SIVASHINSKY, G. I. 1982 Thermal-expansion induced cellular flames. *Combust. Flame* **48**, 211–217.

OLAMI, Z., GALANTI, B., KUPERVASSER, O. & PROCACCIA, I. 1997 Random noise and pole dynamics in unstable front propagation. *Phys. Rev.* E **55** (3), 2649.

PATYAL, A. & MATALON, M. 2018 Nonlinear development of hydrodynamically-unstable flames in three-dimensional laminar flows. *Combust. Flame* **195**, 128–139.

PELCE, P. & CLAVIN, P. 1982 Influence of hydrodynamics and diffusion upon the stability limits of laminar premixed flames. *J. Fluid Mech.* **124** (1), 219–237.

PELCE, P. & CLAVIN, P. 1987 The stability of curved fronts. *Europhys. Lett.* **3** (8), 907–913.

PELCÉ-SAVORNIN, C., QUINARD, J. & SEARBY, G. 1988 The flow field of a curved flame propagating freely upwards. *Combust. Sci. Technol.* **58** (4–6), 337–346.

QUINARD, J. 1984 Limite de stabilité et structures cellulaires dans les flammes de prémélange: étude expérimentale. PhD thesis.

RABAUD, M., COUDER, Y. & GERARD, N. 1988 Dynamics and stability of anomalous Saffman-Taylor fingers. *Phys. Rev.* A **37** (3), 935–947.

RADISSON, B., PIKETTY-MOINE, J. & ALMARCHA, C. 2019 Coupling of vibro-acoustic waves with premixed flame. *Phys. Rev. Fluids* **4** (12), 121201.

RAHIBE, M., AUBRY, N., SIVASHINSKY, G. I. & LIMA, R. 1995 Formation of wrinkles in outwardly propagating flames. *Phys. Rev.* E **52** (4), 3675–3686.

RASTIGEJEV, Y. & MATALON, M. 2006a Nonlinear evolution of hydrodynamically unstable premixed flames. *J. Fluid Mech.* **554** (1), 371–392.

RASTIGEJEV, Y. & MATALON, M. 2006b Numerical simulation of flames as gas-dynamic discontinuities. *Combust. Theor. Model.* **10** (3), 459–481.

SAFFMAN, P. G. & TAYLOR, G. 1958 The penetration of a fluid into a porous medium or Hele-Shaw cell containing a more viscous liquid. *Proc. R. Soc. Lond.* A **245** (1242), 312–329.

SEARBY, G. & QUINARD, J. 1990 Direct and indirect measurements of Markstein numbers of premixed flames. *Combust. Flame* **82** (3–4), 298–311.

SEARBY, G., TRUFFAUT, J.-M. & JOULIN, G. 2001 Comparison of experiments and a nonlinear model equation for spatially developing flame instability. *Phys. Fluids* **13** (11), 3270–3276.

SHARIF, J., ABID, M. & RONNEY, P. D. 1999 Premixed-gas flame propagation in Hele-Shaw cells. In *Spring Technical Meeting, Joint US Sections (15–17 March 1999)*. Combustion Institute, Washington, DC.

SIVASHINSKY, G. I. 1977 Nonlinear analysis of hydrodynamic instability in laminar flames–I. Derivation of basic equations. *Acta Astron.* **4** (11–12), 1177–1206.

SIVASHINSKY, G. I. & CLAVIN, P. 1987 On the nonlinear theory of hydrodynamic instability in flames. *J. Phys.* **48** (2), 193–198.

SMITHELLS, A. & INGLE, H. 1892 XV.–The structure and chemistry of flames. *J. Chem. Soc. Trans.* **61**, 204–216.

SWIFT, D. L. & FRIEDLANDER, S. K. 1964 The coagulation of hydrosols by Brownian motion and laminar shear flow. *J. Colloid Sci.* **19** (7), 621–647.

TAYLOR, G. 1950 The instability of liquid surfaces when accelerated in a direction perpendicular to their planes. I. *Proc. R. Soc. Lond.* A **201** (1065), 192–196.

THUAL, O., FRISCH, U. & HÉNON, M. 1985 Application of pole decomposition to an equation governing the dynamics of wrinkled flame fronts. *J. Phys.* **46** (9), 1485–1494.

TRUFFAUT, J.-M. & SEARBY, G. 1999 Experimental study of the Darrieus–Landau instability on an inverted-'V' flame, and measurement of the Markstein number. *Combust. Sci. Technol.* **149** (1–6), 35–52.

UBEROI, M. S. 1959 Flow field of a flame in a channel. *Phys. Fluids* **2** (1), 72–78.

VAYNBLAT, D. & MATALON, M. 2000a Stability of pole solutions for planar propagating flames. I. Exact eigenvalues and eigenfunctions. *SIAM J. Appl. Maths* **60** (2), 679–702.

VAYNBLAT, D. & MATALON, M. 2000b Stability of pole solutions for planar propagating flames. II. Properties of eigenvalues/eigenfunctions and implications to stability. *SIAM J. Appl. Maths* **60** (2), 703–728.

VILLERMAUX, E. & DUPLAT, J. 2003 Mixing is an aggregation process le mélange est un processus d'agrégation. *C. R. Mecanique* **7** (331), 515–523.

VON LAVANTE, E. & STREHLOW, R. A. 1983 The mechanism of lean limit flame extinction. *Combust. Flame* **49** (1–3), 123–140.

YU, R., BAI, X.-S. & BYCHKOV, V. 2015 Fractal flame structure due to the hydrodynamic Darrieus–Landau instability. *Phys. Rev.* E **92** (6), 063028.

ZELDOVICH, Y. B., ISTRATOV, A. G., KIDIN, N. L. & LIBROVICH, V. B. 1980 Flame propagation in tubes: hydrodynamics and stability. *Combust. Sci. Technol.* **24**, 1–13.